Adsorption-catalysis design with cerium oxide nanorods supported nickel-cobalt-oxide with multifunctional reaction interfaces for anchoring polysulfides and accelerating redox reactions in lithium sulfur battery

Sakibul Azam, Zhen Wei, Ruigang Wang *

Department of Metallurgical and Materials Engineering, The University of Alabama, Tuscaloosa, AL 35487, United States

GRAPHICAL ABSTRACT
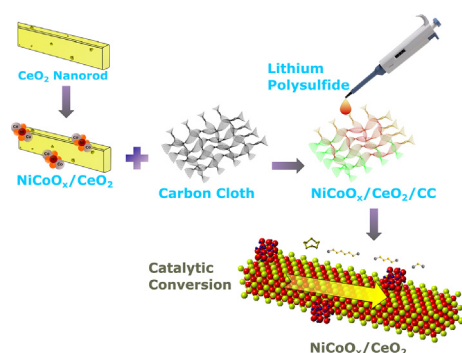
ARTICLE INFO

ABSTRACT

The charge and discharge working mechanisms in lithium sulfur batteries contain multi-step complex reactions involving two-electron transfer and multiple phase transformations. The dissolution and diffusion of lithium polysulfides cause a huge loss of active material and fast capacity decay, preventing the practical use of lithium sulfur batteries. Herein, CeO_2 nanorods supported bimetallic nickel cobalt oxide ($NiCo_2O_x$) was investigated as a cathode host material for lithium sulfur batteries, which can provide adsorption-catalysis dual synergy to restrain the shuttle of polysulfides and stimulate rapid redox reaction for the conversion of polysulfides. The polar CeO_2 nanorods with abundant surface defects exhibit chemisorption towards lithium polysulfides and the excellent electrocatalytic activity of $NiCo_2O_x$ nanoclusters can rev up the chain transformation of lithium polysulfides. The electrochemical results show that the battery with $NiCo_2O_x/CeO_2$ nanorods can demonstrate high discharge capacity, stable cycling, low voltage polarization and high sulfur utilization. The battery with $NiCo_2O_x/CeO_2$ nanorods unveils a high specific capacity of 1236 mAh g^{-1} with a very low capacity fading of 0.09% per cycle after 100 cycles at a 0.2C current rate. Moreover, the excellent performance with high sulfur loading (>5 mg cm^{-2}) verifies a huge promise for future commercial applications.

---

* Corresponding author.
  E-mail address: rwang@eng.ua.edu (R. Wang).

1. Introduction

The increasing consumption and limited availability of fossil fuels, along with the environmental pollution and climate change caused by the increased amount of carbon dioxide emission due to the burning of fossil fuels, have significantly triggered the development of environmentally sustainable energy conversion and storage materials and technologies [1–3]. Lithium Sulfur Batteries (LSBs) have been considered as a promising alternative to replace currently dominating secondary energy storage devices like Li-ion batteries, giving merit to the high theoretical capacity of sulfur (1675 mAh g^{-1}), which is naturally abundant (17th richest element) and environmentally friendly element [4,5]. However, LSBs are not feasible yet for large-scale production and commercialization because of some inherent problems such as: i) sluggish reaction kinetics deriving from insulating S (5 × 10^{-30} S cm^{-1} at room temperature) and its discharge products like insoluble Li$_2$S affecting the rate performance of the battery; ii) the lithium polysulfides dissolution and diffusion in the liquid organic electrolyte and the notorious polysulfide shuttling effect seriously inhibiting long cycle lifetime and causing low utilization of active sulfur; iii) the sulfur expansion (Volume change ∼80%) during cycling caused by the density gap between sulfur (2.07 g cm^{-3}) and lithium sulfide Li$_2$S (1.66 g cm^{-3}) [6–9]; iv) dendrite formation originating from the uneven distribution of lithium ions on the lithium metal surface generating safety concerns [10,11]. The practical requirement of sulfur loading (>5 mg cm^{-2}) also could accompany new challenges like slow reaction kinetics due to increased amount of insulating sulfur, more aggressive polysulfide shuttling effect and blocking of electron transfer channels, and corrosion of lithium metal anode [12].

Over the past few years, several cathode architectures have been proposed by researchers to deal with these inherent problems of LSBs [13–15]. In the early days of LSBs, the most popular strategy was to incorporate carbon/sulfur composite containing high surface area with large pore volume and high electronic conductivity, to be used in encapsulation and shuttling suppression of lithium polysulfides (Li$_2$S$_n$: 4 < n < 8) [16–20]. However, this physical adsorption of polysulfides using non-polar carbonaceous materials is not adequate to sequester the polysulfide shuttling effect, making it difficult to achieve long cycle lifetime. Moreover, the restricted charge transfer between the non-polar carbon and the hydrophilic lithium polysulfide interface has adverse effect on the reaction kinetics. So, to chemically bind the polysulfides, previously, many researchers investigated a variety of novel materials in the form of oxides such as transition metal oxides (V$_2$O$_3$ [21], MnO [22], Fe$_3$O$_4$ [23]), sulfides (Co$_3$S$_4$ [24,25], WS$_2$ [26], FeS [27], SnS$_2$ [28]), nitrides (NbN [29], VN [30,31], TiN [32]) etc. to attach or trap the polysulfides with the cathode host. These polar materials restrict the polysulfide shuttling by chemically binding in their polar surface clinching strong contact and help to obtain long cycle lifetime LSBs. The chemical adsorption also enables the uniform distribution of S and Li$_2$S on the cathode host material ensuring the mitigation of dissolution of lithium polysulfides in the cathode [9]. However, these agglomerated polysulfides on the cathode side cause sluggish reaction kinetics for polysulfide conversion and eventually shuttle towards the lithium anode because of concentration gradient.

Now, having a closer look at the polysulfide conversion, it is a multistep reduction reaction process and can be categorized by **a)** binding and stabilizing the polysulfides, and **b)** electrochemically converting the higher order polysulfides (Li$_2$S$_n$: 4 < n < 8) to lower order polysulfides (Li$_2$S$_2$/Li$_2$S) [33–35]. Almost 75% of the theoretical capacity of LSB comes from the conversion of Li$_2$S$_4$ to Li$_2$S liquid-solid conversion [36,37]. So, only the adsorption syn-

ergy may not be the most influential factor to achieve high-capacity long cycle life LSB. Although the previously mentioned polar materials like transition metal oxides (low catalytic ability), nitrides (aggregation), sulfides (weak affinity) can effectively bind the lithium polysulfides chemically, there is still room for improvement in terms of reaction kinetics for the rapid electrochemical conversion to the electrically insulating insoluble lithium polysulfides. This slow conversion reaction kinetics results in accumulation of polysulfides in the cathode area and the electrolyte, which can dissolve in the electrolyte and cause low utilization of sulfur [9,34]. Moreover, it can cause random deposition of large solid Li$_2$S particles on the cathode host surface, deteriorating the conductivity and subsequent charge-discharge cycling [36]. The situation gets even worse when the polar materials come to a saturation point when it is filled with polysulfides that it can bind, leading to dissolution of remaining polysulfides in the electrolyte. This phenomenon happens particularly in the high sulfur loading condition of >5 mg cm^{-2} for practical use. So, to fully convert all the higher order polysulfides to Li$_2$S by avoiding the dissolution of polysulfides, a catalytic host material component is needed that can accelerate the reaction kinetics and reduce the aggregation and diffusion of polysulfides in the electrolyte. Recently, heterostructure engineering of novel materials for catalytic conversion of polysulfides has been proven as an effective strategy to realize high performance lithium sulfur batteries [38–42]. So, the combination of adsorption-catalysis synergy of a host material can guide us towards the next generation LSBs [9]. The combination of materials with adsorption and catalytic superiority can be an effective strategy, where one material will chemically adsorb the lithium polysulfides in its interface, whereas the other material will provide catalytic support to accelerate the polysulfide conversion reaction kinetics.

Cerium oxide (CeO$_2$) is a promising material that has been previously reported as cathode host material for LSB. CeO$_2$ as a metal catalyst support material or a catalytically active material due to reversible Ce^{4+}/Ce^{3+} transformation was investigated previously because of its remarkable CO oxidation capability [43,44], oxygen storage capability [45,46], excellent redox activity [47,48] and facile surface oxygen mobility [49,50]. CeO$_2$ with well-defined nanorod shape has tremendous ability to exchange surface oxygen and exhibits strong anchoring and/or "alloying" with metal catalyst clusters being a host (support) material promoting dispersion and thermal stability of the catalysts. For instance, Cao et al. designed a CeO$_2$/ultrathin nitrogen doped carbon shell structure to improve both the physical and chemical confinement of lithium polysulfides where the carbon shell provides the physical confinement and the CeO$_2$ provides the chemical binding of polysulfides [51]. Zhang et al. synthesized CeO$_2$/rGO composite material using a spray-drying process to block the dissolution of polysulfides in the electrolyte [52]. Shen et al. fabricated a composite of ketjen black decorated with homogenous distribution of CeO$_2$ nanodots as cathode host for LSB [53]. Previously, our group investigated **1)** hydrothermal synthesis and decoration of CeO$_2$ nanorods on flexible carbon cloth as cathode host material [54], **2)** CeO$_2$ nanorods on cellulose derived carbon as effective interlayer [55], **3)** surface engineered shape controlled CeO$_2$ nanorods, nanoctahedra, nanocubes [56] as cathode host materials, and **4)** chemically etched CeO$_{2-x}$ nanorods to increase the concentration of surface oxygen vacancy and other defects [57] as cathode host material to design novel LSBs. The polar CeO$_2$ nanorods with surface oxygen functional group containing surface defects in the form of oxygen vacancies with Ce^{3+} "defect" sites, exposing (110)/(100) faces or defected (111) faces can bind lithium polysulfide anions and trap the polysulfides effectively. The oxygen vacancy defects on the surface of CeO$_2$ nanorods can also provide active sites for redox reaction during cycling and escalate the ion insertion/extraction

processes [58]. Furthermore, the abundance of oxygen vacancies provides polysulfide binding sites and facilitate catalytic effect towards polysulfide conversion reaction by generating in-situ thiosulfate $[S_2O_3]^{2-}$ and polythionate $[SO_3S_2SO_3]^{2-}$ species.

Bimetallic catalysts with cobalt component have long been recognized as efficient catalyst for oxygen evolution reaction (OER) [59] and cathode catalyst for Li-O₂ batteries [60] because of their highly flexible electronic structure (Co^{2+} and Co^{3+}) and composition and excellent catalytic activity. Although monometallic Co_3O_4 is already very catalytically active itself, doping it with another transition metal can promote the catalytic activity further by tuning the electronic state, making it a tremendous choice for supercapacitors [61–64], pseudocapacitors [65], Li ion batteries [66,67]. Nickel cobalt bimetallic oxides ($NiCo_2O_4$) having spinel structure with cobalt cations occupying both tetrahedral and octahedral sites and nickel cations in octahedral sites, have been investigated previously to design LSBs [68–72]. $NiCo_2O_4$ can catalytically convert the lithium polysulfides by the interaction of metal surface or oxygen ions with S_x^{2-} and helps the Li-ion on its surface to reduce the energy barrier for diffusion [72,73]. The energetically favorable (3 1 1) plane of the spinel $NiCo_2O_4$ can also adsorb the polysulfides significantly and accelerate the reactions for forming thiosulfate $[S_2O_3]^{2-}$ and polythionate $[SO_3S_2SO_3]^{2-}$ species [72]. Moreover, monometallic oxides typically possess low conductivity, whereas the conductivity of $NiCo_2O_4$ is in the significant range of 0.1–0.3 S cm^{-1} because of the coexistence of Ni^{3+}/Ni^{2+} and Co^{3+}/Co^{2+} redox couples, which are a few orders higher than Co_3O_4 monometallic oxide (3.1×10^{-5} S cm^{-1}) [72,74,75]. Previously, Xiong et al. designed a $NiCo_2O_4$/rGO coated separator for catalytic conversion of polysulfides and improved the cycle stability and areal capacity even in high sulfur loading condition of 6 mg cm^{-2} [73]. Fang et al demonstrated metal organic framework derived bimetallic oxide ($NiCo_2O_4$) in porous carbon as efficient sulfur host for LSBs and investigated the binding mechanism of $NiCo_2O_4$ with polysulfides by ex-situ XRD and DFT study [74]. Iqbal et al. fabricated hollow microtubes with $NiCo_2O_4$ nanosheets where $NiCo_2O_4$ provides a large functional surface for polysulfide adsorption and catalytic conversion [76]. Gao et al. demonstrated carbon free sulfur immobilizer by $NiCo_2O_4$ nanofibers where the fiber structure provides good conductivity, strong adsorption ability and high electrocatalytic activity [75]. In addition, Liu et al. demonstrated $NiCo_2O_4$ nanofiber array grown on carbon cloth as electrocatalyst for lithium polysulfide conversion achieving excellent performance.

Considering the above discussions, herein, we introduce $NiCo_2O_x/CeO_2$ as the sulfur host with dual adsorption-catalysis mechanism, where the CeO_2 nanorods act as support or host for catalytic $NiCo_2O_x$ nanoclusters (Fig. 1). 10 wt% Ni-Co bimetallic oxide with the atomic ratio of nickel to cobalt as 1:2 onto CeO_2 nanorods via hydrothermal supported precipitation-deposition method is designated thereinafter as 10 wt% $NiCo_2O_x/CeO_2$ NR. The proposed $NiCo_2O_x/CeO_2$ NR dual-functional host material has the following advantages: **i)** Adsorption synergy: CeO_2 nanorods as polar host material with oxygen functional group can adsorb and bind the lithium polysulfides during the cycling to deal with the polysulfide shuttling effect, and **ii)** Catalysis synergy: $NiCo_2O_x$ nanoclusters decorated on CeO_2 NR host can provide electrocatalytic effect to accelerate the polysulfide conversion reaction and improve the sluggish redox kinetics. To the best of our knowledge, $NiCo_2O_x/CeO_2$ NR has never been deployed as sulfur host for LSBs. In this report, the $NiCo_2O_x/CeO_2$ nanorods composite shows excellent performance with significant cycling stability and noteworthy rate performance. The cell with $NiCo_2O_x/CeO_2$ NR presents a high initial discharge capacity of 1236 mAh g^{-1} at 0.2C current rate and can retain a high discharge capacity of 1120 mAh g^{-1} after 100 cycles, with a capacity fading rate of only 0.09% per cycle.

Moreover, it exhibited initial discharge capacity of 931 mAh g^{-1} at 1C.

2. Experimental section

Synthesis of CeO₂ nanorods: A facile hydrothermal method was employed to synthesize CeO_2 nanorods support material [77]. First, a solution of 88 mL 0.1 M $Ce(NO_3)_3 \cdot 6H_2O$ was prepared in a Teflon-lined autoclave with a volume of 200 mL. Then, 8 mL of aqueous solution of 6.0 M NaOH was added dropwise with continuous stirring with a glass rod into the solution inside the autoclave within 15 s, followed by sealing of the autoclave. Then hydrothermal reaction was carried out by placing the autoclave inside a box furnace, where the temperature was controlled at 90 °C for 48 h. After the hydrothermal processing, the precipitates were cleaned with deionized water (3 times) and ethanol (2 times) in a vacuum filter to prevent agglomeration and to get rid of any residual ions. The samples were then dried completely to remove water residue in vacuum oven at 60 °C for 12 h to acquire CeO_2 nanorods powder.

Fabrication of NiCo₂Oₓ/CeO₂ NR: The CeO_2 nanorods suspension was first prepared by putting 0.9 g of CeO_2 nanorods powder into a mixture of 96 mL absolute ethanol and 4 mL of deionized water and vigorously stirred magnetically to make a homogenous suspension. Then $Ni(NO_3)_2 \cdot 6H_2O$ (0.1645 g) and $Co(OAc)_2 \cdot 4H_2O$ (0.2821 g) powders were added under vigorous stirring and dissolved in the CeO_2 suspension at room temperature. Then, 0.5 mL of aqueous ammonium hydroxide was mixed with the solution slowly. The solution was then aged at 80 °C for 20 h followed by transferring into a Teflon lined stainless steel autoclave. The hydrothermal reaction was activated in a box furnace at 150 °C for 1 h. After the hydrothermal reaction, the as obtained solution was transferred into a glass beaker and the water was evaporated by drying in an oven at 80 °C for 24 h. After drying, the powders were ground in a mortar and pestle to make them fine and subsequently calcined at 400 °C for 5 h to obtain $NiCo_2O_x/CeO_2$ NR.

Cell assembly: The cathode host material was prepared by pasting a slurry on a carbon cloth (circular 15 mm diameter) using *N*-methyl-2-pyrrolidone consisting of $NiCo_2O_x/CeO_2$ NR powder, super P conductive carbon black and PVDF binder in the ratio of 7:1:2. The powders were mixed well using a vortex mixer. Then the mixed powders were soaked with *N*-methyl-2-pyrrolidone and magnetically stirred overnight vigorously to make a uniform slurry with appropriate viscosity. Then the slurry was coated on a circularly cut carbon cloth (CC) current collector with an area of ∼1.5 cm². The NMP was evaporated by drying the coated CC at 60 °C for 12 h in an oven under vacuum environment. The piece of carbon cloth was weighted before and after slurry coating to determine the mass of $NiCo_2O_x/CeO_2$ NR. The loading of $NiCo_2O_x/CeO_2$ NR was calculated as 0.75 mg cm^{-2}.

All the cells were assembled inside an argon filled glovebox (VTI Vacuum Technology Inc.). The glovebox was maintained at a minimal moisture and oxygen content <0.1 ppm. CR2032 type coin cells from MTI corporation were used. The as-prepared $NiCo_2O_x/CeO_2$ NR slurry coated carbon cloth (15 mm diameter) was used as cathode host material, Celgard 2500 polypropylene separator (19 mm diameter) was used with 55% porosity and 0.064 pore size distribution, and lithium foil (15 mm diameter) was used as anode material.

The sulfur was introduced in the cathode host matrix by dropping lithium polysulfide catholyte. For this step, a blank electrolyte was prepared first by putting together a solution of 1 M lithium bis (tri-fluoromethanesulfonyl)imide (LiTFSI) in 1, 2-dimethoxyethane (DME) and 1, 3- dioxolane (DOL) (1:1 by volume ratio) containing 1 wt% lithium nitrate ($LiNO_3$). Then sublimed sulfur and lithium sulfide (Li_2S) in appropriate ratio were chemically reacted by stir-
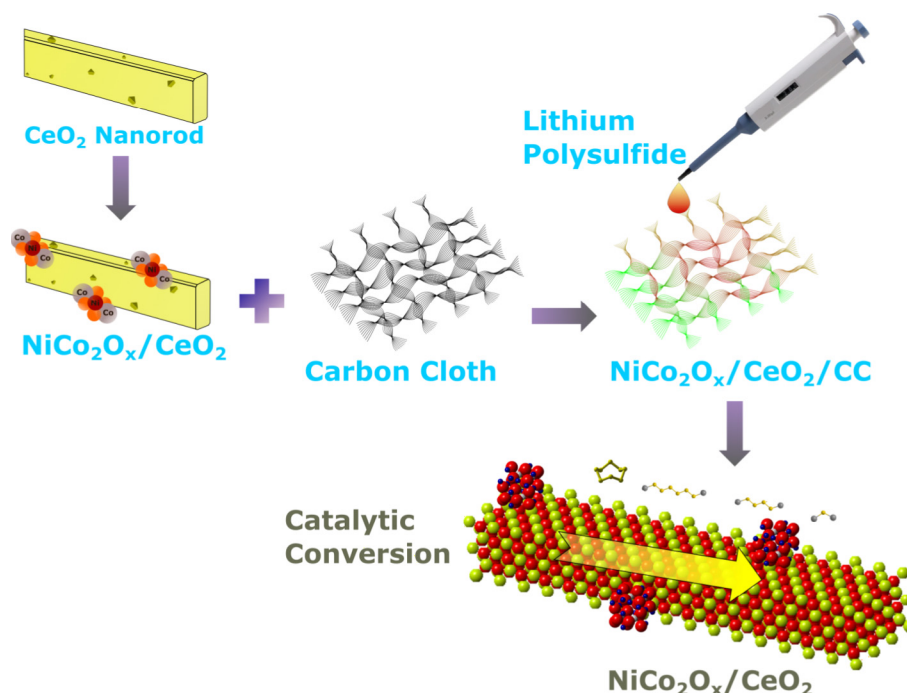
Fig. 1. Schematic illustration of the preparation processes of LSB using $NiCo_2O_x/CeO_2$ NR as cathode host showing the dual functionality of adsorption-catalytic conversion of lithium polysulfides.

ring in the as prepared blank electrolyte at 60 °C for 12 h under argon environment. To assemble the coin cell battery, first, 20 μL of the polysulfide catholyte was dropped on the $NiCo_2O_x/CeO_2$ NR coated carbon cloth to obtain 2 mg sulfur loading (1.33 mg cm^{-2}, higher amount of catholyte for higher sulfur loading). After uniformly distributing the catholyte on the cathode host, the DOL: DME solvent was evaporated naturally. The separator was wetted by 60 μL of the blank electrolyte. After putting the lithium foil, the cells were assembled and sealed using Gelon hydraulic crimper. This instrument can also be mounted with a disassembling die to disassemble the cells for post cycling analysis.

Polysulfide adsorption test: A 0.05 M solution of Li_2S_6 catholyte was prepared first as the process discussed above. The solution was then diluted to 5 mM. 40 mg of $NiCo_2O_x/CeO_2$ NR and/or CeO_2 nanorods powder were added in the 1 mL of the solution inside the glovebox and observed for discoloration while aging.

Material characterization: The morphological distribution of the particles was done in transmission electron microscope (TEM, Tecnai F20) operating at a field emission of 200 kV. The $NiCoO_x/CeO_2$ nanorods powders were ultrasonicated in absolute ethanol for 30 min and then the dispersion was dropped on a carbon coated copper grid using a glass pipette followed by room temperature drying. Philips X'Pert MPD X-ray diffractometer with Cu Kα radiation (λ = 1.5405 Å) operating at 45 kV and 40 mA was used for X-ray diffraction of the sample by keeping the powder sample on a zero-background quartz sample holder. The goniometer supported angular movement provided X-ray data taken within the 2θ range of 10° to 80° with a controlled step size of 0.5°/min. The peak position indexing was done in HighScore plus software equipped with JCPDS-JCDD database. Horiba LabRAM HR 800 Raman spectrometer using 532 nm laser was used operating in the 100 to 1200 cm^{-1} spectral window to obtain Raman spectra. The Raman instrument was calibrated using a single crystal silicon wafer as the reference (520.7 cm^{-1}). X-ray photoelectron spectroscopy (XPS) was conducted by VersaProbe 5000 spectrometer with monochromatic Al Kα (hν = 1486.6 eV) radiation at a working pressure of <8 × 10^{-10} Torr. As a reference for standard calibration, the carbon C 1s line (284.8 eV) was used. Thermo Scientific Apreo FE-SEM was used to collect the scanning electron microscopy (SEM) images with the accelerated voltage ranging from 1 kV to 30 kV. The instrument is also equipped with EDAX to perform Energy Dispersive X-ray Spectroscopy (EDS) with elemental mapping and data processing software APEX-EDS.

Electrochemical characterization: The galvanostatic charge-discharge experiments were done in Neware battery tester that comes with BTS software to program the current density, cycle numbers etc. The Gamry instrument Interface-1000 potentiostat/-galvanostat/ZRO was used to conduct electrochemical impedance spectroscopy (EIS) and cyclic voltammetry (CV) measurements.

3. Results and discussion

3.1. Microstructure analysis and characterization

The CeO_2 nanorods were prepared using a simple hydrothermal process [78]. Then the obtained CeO_2 nanorods were further processed with nickel and cobalt source using solution decomposition method to get 10 wt% $NiCo_2O_x/CeO_2$ NR as previously reported [43]. The morphology and structural characterization of $NiCo_2O_x/CeO_2$ NR emerged in Fig. 2. Fig. 2a shows the SEM image of the morphology of the $NiCo_2O_x/CeO_2$ NR coated on the carbon cloth current collector and its corresponding EDS elemental mapping. The carbon cloth was fully decorated with the $NiCo_2O_x/CeO_2$ nanorods based slurry material. The slurry material coated on highly conductive carbon cloth current collector provides a strong binding, ensuring rapid electron transport. The $NiCo_2O_x/CeO_2$ NR provide abundant active sites to anchor polysulfides and catalytic conversion of polysulfides to improve sulfur utilization. The elemental mapping shown in Fig. 2a exhibits the uniform spreading of the elements Ni, Co, Ce, O on the carbon cloth scaffold. The EDS analysis was also performed to quantify the chemical composition of the supported $NiCo_2O_x$ catalysts on CeO_2 nanorods as shown in the EDS spectrum of Fig. 2b.
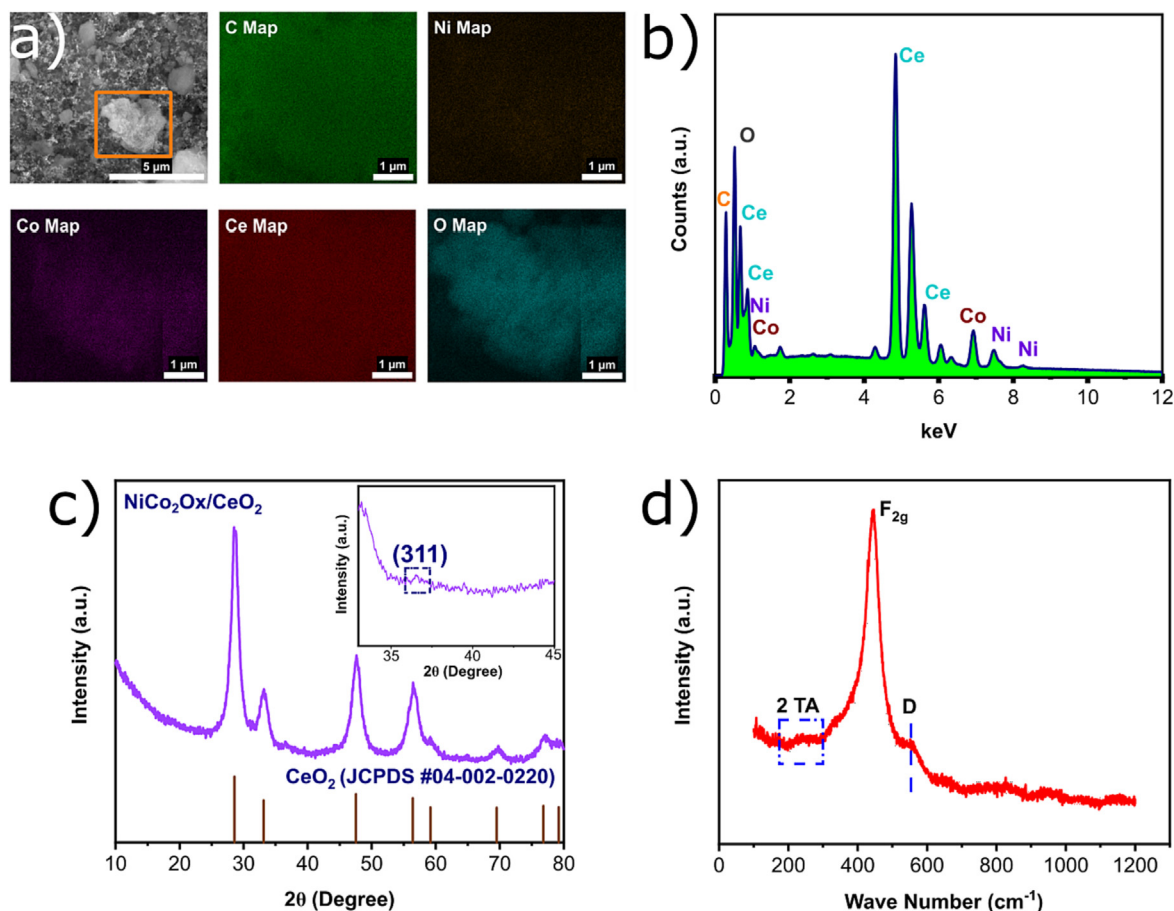
Fig. 2. a) SEM image of $NiCo_2O_x/CeO_2$ NR slurry coated on carbon cloth and its corresponding EDS elemental mappings of C, Ni, Co, Ce, O in (a) and EDS spectrum in (b). c) XRD pattern of CeO_2 nanorods supported $NiCo_2O_x$ with enlarged region shown in the inset. d) Raman spectrum of $NiCo_2O_x/CeO_2$ NR.

The powder X-ray diffraction was performed to analyze the crystal structure of $NiCo_2O_x/CeO_2$ NR. In Fig. 2c, the XRD pattern shows the diffraction peaks of cubic crystal fluorite group of CeO_2 phase with Fm-3m space group (JCPDS #04-002-0220). The inset plot of Fig. 2c displays the magnified regions of the XRD pattern from 2θ degree 30° to 45°, in which the (3 1 1) reflection peak may have derived from cobalt (II, III) oxide i.e. Co_3O_4 (JCPDS #71-0816) [43]. So, the combined results of EDX (Fig. 2b) and XRD (Fig. 2c) analysis indicate that a strong interaction occurs between the nickel cobalt bimetallic oxide and CeO_2 support possibly by cation diffusion.

Raman spectroscopy was done to investigate cation coordination by the existing elements and to analyze the oxygen vacancy concentration of the $NiCo_2O_x/CeO_2$ NR powder. Fig. 2d shows the Raman spectrum of CeO_2 nanorods supported nickel cobalt bimetallic catalyst. The main peak around 444 cm^{-1} corresponds to triply degenerate symmetric stretching vibration mode F_{2g} of CeO_2 fluorite structure [43,44,54,55,79]. The peak at 237 cm^{-1} denotes the second-order transverse acoustic mode of cerium oxide (CeO_2) [80]. The D-band at 550 cm^{-1} generated from the defect indicates oxygen vacancies originating from the surface defects of the CeO_2 nanorods [57]. This extrinsic oxygen vacancy can also stem from incorporation of bivalent or trivalent metal cation (Co^{2+}, Co^{3+}, Ni^{2+}) into CeO_2 support lattice.

TEM images shown in Fig. 3 exhibit the nanorod structure of CeO_2 as support with a varying diameter from 5 to 10 nm and the length of the nanorods ranging from 50 to 100 nm with $NiCo_2O_x$ nanoclusters (circled) decorated on it. From the image it can be observed that the CeO_2 nanorod supported $NiCo_2O_x$ catalyst con-

tains rough surface and significant amount of surface defects. Moreover, bimetallic $NiCo_2O_x$ cluster is observed on the CeO_2 nanorod surface.

X-ray photoelectron spectroscopy (XPS) was applied to observe the chemical composition and oxidation state from the surface of $NiCo_2O_x/CeO_2$ NR. Fig. 4 **(a-c)** show the XPS spectra of Ce 3d, Ni 2p and Co 2p respectively for the CeO_2 nanorods supported bimetallic $NiCo_2O_x$ sample. In Fig. 4a, the u and v peaks represent the spin orbital splitting of Ce $3d_{5/2}$ and Ce $3d_{3/2}$ [55,81]. The Ce 4f electron configuration of Ce^{4+} species produce these u'''/v''' and u''/v'' pairs of peaks. The two electron configuration of Ce^{3+} species results in the v' peak [82]. The Ni 2p spectrum of the $NiCo_2O_x/CeO_2$ is shown in Fig. 4b where the spin-orbital coupling Ni $2p_{1/2}$ and $2p_{3/2}$ at 871.28 eV and 853.42 eV respectively assigned to Ni^{2+} species [43,83]. For the Co 2p spectrum in Fig. 4c, the $2p_{3/2}$ peak can be deconvoluted into two substantial components of Co^{2+} and Co^{3+} at the binding energy of 779.31 eV and 778.14 eV respectively. So, the XPS analysis confirms the presence of Ni^{2+} for Ni and Co^{2+} and Co^{3+} for Co on the CeO_2 nanorods support. Moreover, as shown in **Fig. S1**, the pristine O 1s spectrum of $NiCo_2O_x/CeO_2$ NR can be split into oxygen lattice (O_L peak) at 527.82 eV and surface oxygen vacancies (O_V peak) centered at 529.66 eV which proves the existence of oxygen vacancies [84–87]. These oxygen vacancies play a critical role in the catalytic conversion of lithium polysulfides. The comparative amount of oxygen vacancies can be calculated from the ratio of the peak area of O_V to the total area of the deconvoluted O_L and O_V peaks ($\frac{O_V}{O_L+O_V}$). The amount of oxygen vacancies in $NiCo_2O_x/CeO_2$ was calculated as 37.61%.
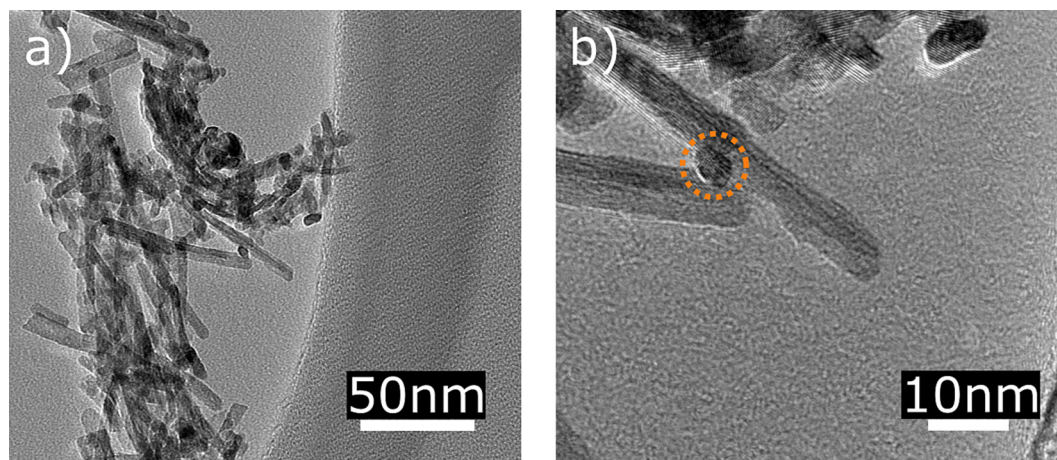
Fig. 3. a–b) TEM images of CeO$_2$ nanorods supported NiCo$_2$O$_x$ clusters.
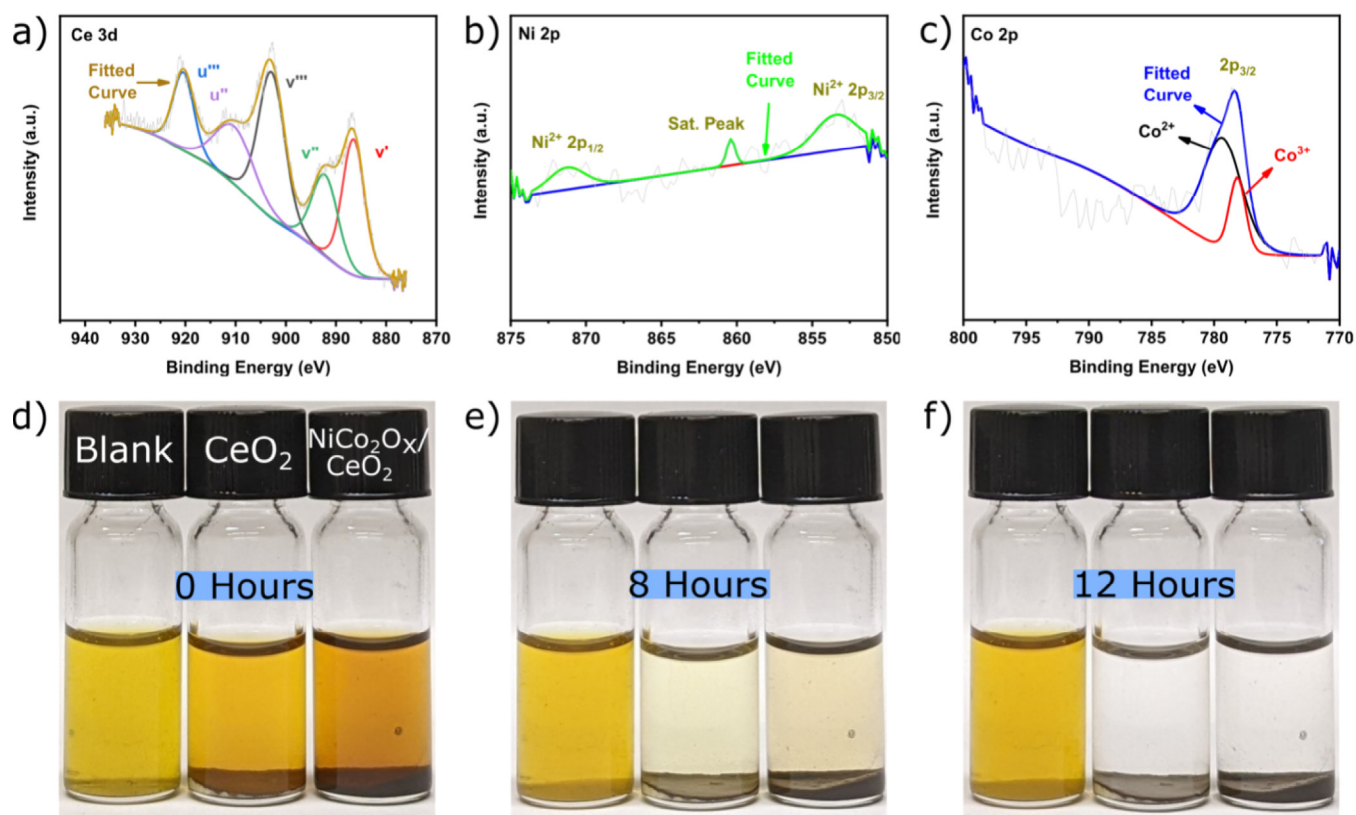

Fig. 4. (a–c) XPS spectra of a) Ce 3d for CeO$_2$ nanorods support and b) Ni 2p and c) Co 2p for nickel cobalt bimetallic oxide nanoclusters. (d–f) Polysulfide adsorption experiment for different times (0 h, 8 h, 12 h) with optical image of blank Li$_2$S$_6$ solution and CeO$_2$ and NiCo$_2$O$_x$/CeO$_2$ NR dispersed in Li$_2$S$_6$ solution.

To visually verify the interfacial interaction between NiCo$_2$O$_x$/CeO$_2$ NR and lithium polysulfides, 40 mg of each of CeO$_2$ nanorods powder and NiCo$_2$O$_x$/CeO$_2$ NR powders were dispersed into 1 mL of 5 mM Li$_2$S$_6$ in DOL/DME (volume ratio 1:1) solution respectively, following 12 h of aging at room temperature. The color change of the solutions was compared with blank solution after aging for 12 h as shown in Fig. 4 **(d-f)**. The solutions with both CeO$_2$ and NiCo$_2$O$_x$/CeO$_2$ NR turned from yellow to transparent gradually in 12 h whereas the blank polysulfide remained the same, revealing the strong adsorption ability of CeO$_2$ and NiCo$_2$O$_x$/CeO$_2$ NR. It is evident that, NiCo$_2$O$_x$/CeO$_2$ NR can suppress the lithium polysulfide diffusion and enhance sulfur utilization.

3.2. Cell electrochemical performance

The symmetrical batteries were assembled by putting separator between the two similar NiCo$_2$O$_x$/CeO$_2$ NR based electrodes and dropping Li$_2$S$_6$ catholyte on each electrode to examine the contribution of NiCo$_2$O$_x$/CeO$_2$ NR in redox kinetics of liquid-liquid conversion of lithium polysulfides (Fig. 5 **a-b**). The cyclic voltammetry (CV) ranging from −1 V to 1 V with a scanning rate of 1 mV s^{-1} (Fig. 5a) and 50 mV s^{-1} (Fig. 5b) determines the polarization curves for the symmetric cells. The polarization contribution comes from the Li$_2$S$_6$ redox current dominantly, and a minor current came from the capacitive contribution. In both Fig. 5 **a-b**,
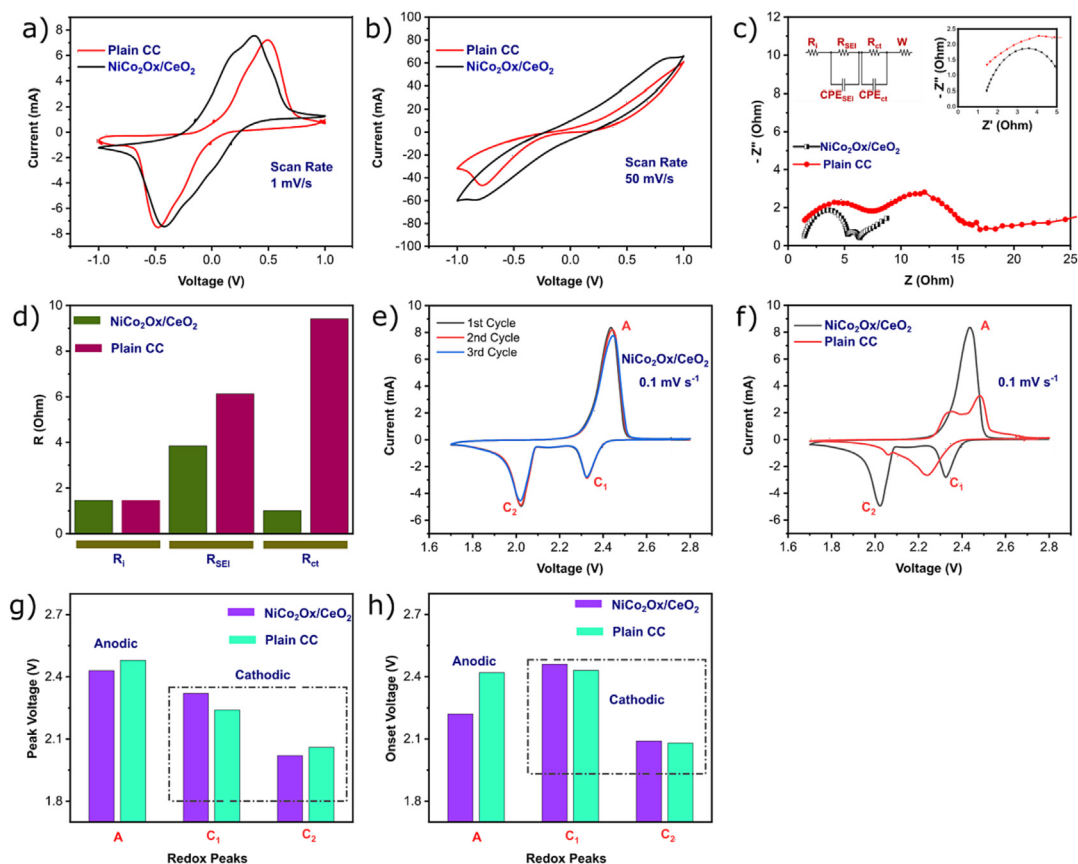
Fig. 5. (a-b) Symmetric CV polarization curves of Li_2S_6 – Li_2S_6 at the scan rate of 1 mV/s in (a) and 50 mV/s in (b) with and without $NiCo_2O_x/CeO_2$ NR. c) Nyquist plot of the cells with corresponding equivalent circuit model. d) Calculated resistance values from Nyquist plot. e) Cyclic Voltammetry (CV) of the cell with $NiCo_2O_x/CeO_2$ NR at a potential sweep rate of 0.1 mV s^{-1}. f) CV curves, g) peak voltages and h) redox onset potentials of the cells with and without the $NiCo_2O_x/CeO_2$ NR at 0.1 mV s^{-1}.

it is evident that the plain carbon cloth (CC) electrodes give out very weak intensity of polarization curves with lower capacitive current, whereas, introducing the electrodes with $NiCo_2O_x/CeO_2$ NR increased current density of polarization. These symmetric CV measurements demonstrate that CeO_2 supported bimetallic $NiCo_2O_x$ facilitates the catalytic conversion reaction of lithium polysulfides, possibly by providing abundant catalytically active surface sites. Considering the contribution from the electrodes only, the $NiCo_2O_x/CeO_2$ NR induces enhanced kinetic redox reaction of polysulfides conversion enabled by fast charge transfer. This affirms the strong chemisorption of polar CeO_2 for soluble polysulfides and contribution from $NiCo_2O_x$ in promoting the conversion. This ability of $NiCo_2O_x/CeO_2$ NR to accelerate charge transfer was further demonstrated by electrochemical impedance spectroscopy (EIS). Fig. 5c shows the Nyquist plot for the cells with $NiCo_2O_x/CeO_2$ NR on carbon cloth ($NiCo_2O_x/CeO_2/CC$) cathode and bare CC cathode within the frequency range from 100000 Hz to 0.1 Hz using the equivalent circuit model shown in the inset figure. In the high frequency region, the X-intercept of the Nyquist plot signifies the ohmic resistance (R_i) of the cell. The first semicircle in the high frequency region determines the insulating solid electrolyte interphase (SEI) layer resistance denoted as R_{SEI} followed by the semicircle in the middle frequency region determines the charge transfer resistance (R_{ct}) at the electrode/electrolyte interface. The R_{ct} semicircle reveals reduction reaction kinetics in the sulfur cathode which represents the higher order (Li_2S_n: 4 < n < 8) to lower order (Li_2S_2/Li_2S) lithium polysulfide conversion. The R_{ct} of the cells with $NiCo_2O_x/CeO_2$ demonstrates a significant drop compared with plain carbon cloth cells, indicating faster charge transfer reaction kinetics at the $NiCo_2O_x/CeO_2$ NR – polysulfide than the bare carbon

cloth – polysulfide interface. Both the cells show the impedance of only 1.46 Ohms (Table 1). However, the R_{SEI} and R_{ct} (3.85 and 1.01 Ohms respectively) of the cell with $NiCo_2O_x/CeO_2$ NR were considerably lower than the cell with bare carbon paper (6.13 and 9.42 Ohms respectively). This almost 90% lower R_{ct} of the cell with $NiCo_2O_x/CeO_2$ NR further substantiates the improved reaction kinetics of polysulfide conversion by effectively reusing the dissolved active materials. The quantitative comparison of resistive parameters is shown in Fig. 5d and given in tabulated form in Table 1.

The expedited polysulfide redox reaction was further investigated by CV curves derived from the Li-S cell using $NiCo_2O_x/CeO_2$ NR to understand the solid-liquid-solid transformation (Fig. 5 e-f). Fig. 5e shows the CV curve of the battery with $NiCo_2O_x/CeO_2$ NR at a scan rate of 0.1 mV s^{-1} with the potential range of 1.7 to 2.8 V vs Li^+/Li. The cell displays two cathodic peaks C_1 and C_2 at 2.32 V and 2.02 V respectively and one anodic peak A at 2.43 V, which resembles the typical charge-discharge of a LSB. The cathodic peak C_1 at 2.32 V corresponds to the reduction of elemental cycloocta sulfur S_8 to soluble higher order lithium polysulfides (Li_2S_n: 4 < n < 8), and the cathodic peak C_2 at 2.02 V determines the conversion of higher order to lower order lithium polysulfides

Table 1
EIS resistance analysis.

Cell	R_i (Ohms)	R_{SEI} (Ohms)	R_{ct} (Ohms)
$NiCo_2O_x/CeO_2/CC$	1.46	3.85	1.01
Plain CC	1.46	6.13	9.42

(Li$_2$S$_2$/Li$_2$S). The anodic peak A indicates the reverse process, from Li$_2$S to S$_8$. The cathodic peak C$_2$ has the most importance since this conversion step determines the catalytic conversion of polysulfides and ultimately the enhanced performance of the battery. The three CV cycle curves with sharp and high charge-discharge peaks almost overlap each other with no potential shift, indicating fast electron/ion transfer process, high reversibility and cycling stability of the NiCo$_2$O$_x$/CeO$_2$ NR based cell. Fig. 5f compares the CV profiles of cells with NiCo$_2$O$_x$/CeO$_2$ NR and bare carbon cloth at a scan rate of 0.1 mV s^{-1} with the potential range of 1.7 to 2.8 V vs Li$^+$/Li. Because of the slow redox kinetics of polysulfides in bare carbon cloth, the cell revealed broad peaks including a shoulder peak in anodic scan with high polarization. The CV profile of bare carbon cloth possessed two cathodic peaks C$_1$ and C$_2$ at 2.24 V and 2.06 V respectively and an anodic peak A at 2.48 V containing a shoulder peak at 2.35 V. The second cathodic peak C$_2$ of the battery with NiCo$_2$O$_x$/CeO$_2$ NR is strikingly higher than the one in the cell with bare carbon cloth, demonstrating a superior polysulfide conversion capability by NiCo$_2$O$_x$/CeO$_2$ NR nanorods. It is clear that the battery with NiCo$_2$O$_x$/CeO$_2$ NR showed significantly sharper redox peaks and mitigated polarization. Moreover, the lower overpotential implies fast reaction kinetics of the battery after introducing NiCo$_2$O$_x$/CeO$_2$ NR. The redox potential quantification is shown in Fig. 5h to study the accelerated polysulfide redox reaction. The cell with NiCo$_2$O$_x$/CeO$_2$ NR has elevated onset potentials of cathodic discharge peaks and declined anodic charged peak compared to bare carbon cloth cell, implying the promotion of redox kinetics by the electrocatalytic effect of CeO$_2$ supported bimetallic NiCo$_2$O$_x$ catalyst. The results demonstrate that the NiCo$_2$O$_x$/CeO$_2$ NR shows adsorption-catalysis dual synergy by sequestering the polysulfide shuttle effect and accelerating the conversion of polysulfide actively.

Another important parameter for long cycling performance LSBs is the Li ion diffusion coefficient (D$_{Li+}$). To compare the diffusion coefficient D$_{Li+}$ of the cells with bare carbon cloth and with NiCo$_2$-O$_x$/CeO$_2$ NR, a series of CV tests were performed at different scan rates as shown in Fig. 6. Generally speaking, the redox reaction of the battery is accelerated, and the polarization of the battery improves with the increase of scanning speed due to the mass transfer limitation. The Randles-Sevcik equation is given by the peak current density $I_p = 2.69 \times 10^5 n^{1.5} A D_{Li+}^{0.5} C v^{0.5}$, where n is the number of charge transfer, C represents the concentration of the electrolyte, A represents the electrode area and v is the CV scan rate [75]. Since the concentration of polysulfide C and the charge transfer n is constant, the D$_{Li+}$ can be calculated from the slope of the linearly fitted curve of the peak current (I_p) vs. square root of scan rate ($v^{0.5}$) [88,89]. It is observed in Fig. 6 **c-d** that the Li ion diffusion coefficient D$_{Li+}$ for the cell with NiCo$_2$O$_x$/CeO$_2$ for anodic peak A and the cathodic peaks C_2 is higher with larger slope than those of the bare CC cells indicating mitigation of polarization by NiCo$_2$O$_x$/CeO$_2$ NR. The slope for first cathodic peak C$_1$ is almost equivalent for both the batteries, which is consistent with the CV curve of Fig. 5f. Since, the NiCo$_2$O$_x$/CeO$_2$ NR triggers the catalytic conversion of polysulfides on the second discharge plateau, hence the Li$^+$ diffusion improves for anodic peak A and cathodic peak C$_2$. For better visualization of the slopes to compare between cell with NiCo$_2$O$_x$/CeO$_2$ and plain CC, the linearly fitted lines for A, C$_1$ and C$_2$ are given in **Fig. S2**. The calculated values of D$_{Li+}$ is shown in **Table S1**. Compared with the plain CC, the cell with NiCo$_2$O$_x$/CeO$_2$ NR shows higher D$_{Li+}$ values for anodic peak A and cathodic peak C$_2$, which further indicates improved Li ion diffusion and reduced electron transfer barrier through the NiCo$_2$O$_x$/CeO$_2$ NR heterostructure providing fast Li ion transport pathway. The abundant oxygen vacancy defect on the CeO$_2$ nanorods and the exposed NiCo$_2$O$_x$/CeO$_2$ NR heterostructure ensures sufficient electrolyte

wetting and affinity which makes this favorable Li$^+$ transfer. The catalytic conversion of polysulfides by NiCo$_2$O$_x$/CeO$_2$ NR opens pathway for Li ion transmission channel and ensures instantaneous transfer of lithium ions.

Electrochemical performances of NiCo$_2$O$_x$/CeO$_2$ NR with 2 mg sulfur loading (1.33 mg cm^{-2}) are shown in Fig. 7. Fig. 7a illustrates the charge discharge curve of lithium sulfur battery with NiCo$_2$O$_x$/CeO$_2$ for various cycles within the voltage range of 2.8 V and 1.7 V versus Li$^+$/Li at 0.2C current rate where 1C = 1675 mA g^{-1} of sulfur. Like the CV curve of Fig. 5e, the two-plateau discharge curve and the single plateau charge curve are present. The first and second discharge plateau designate the conversion of S$_8$ to soluble long chain lithium polysulfides (Li$_2$S$_n$: 4 < n < 8) and the transformation of Li$_2$S$_n$ to insoluble final discharge products Li$_2$S$_2$/Li$_2$S respectively. The initial discharge capacity at 0.2C was achieved at 1236 mAh g^{-1}. After 100 cycles, the reversible capacity was recorded at 1120 mAh g^{-1}. The excellent sulfur utilization was attributed to the adsorption-catalysis synergy of NiCo$_2$O$_x$/CeO$_2$ NR, retaining 95.8% of the initial discharge capacity after 100 cycles with a capacity decay rate of only 0.09% per cycle. Specially in the charge discharge curve, even after 100 cycles, the voltage difference between the long discharge plateau is almost same, demonstrating very low polarization and fast redox conversion kinetics. To understand the adsorption-catalysis effect of NiCo$_2$O$_x$/CeO$_2$ NR, Fig. 7b compares the galvanostatic charge-discharge curves of cathode host made of NiCo$_2$O$_x$/CeO$_2$ NR, CeO$_2$ nanorods and bare CC. The initial discharge capacity of the cell with bare CC host shows a very low capacity of 628 mAh g^{-1} at 0.2C. This low specific capacity stems from the absence of any polar materials with strong polysulfide adsorption capability to prevent the polysulfide diffusion and any electrocatalytic material to accelerate polysulfide conversion. Adding CeO$_2$ nanorods slurry in the carbon cloth improves the discharge capacity to 1106 mAh g^{-1}, which is almost 76% increase than the cell with pure carbon cloth. This significant improvement came from the chemisorption of CeO$_2$ towards the lithium polysulfides. Decorating the CeO$_2$ nanorods with electrocatalytic NiCo$_2$O$_x$ nanoclusters further enhanced the capacity to 1236 mAh g^{-1}, which is almost 97% increase than the cell with bare carbon cloth. The capacity almost doubled with the introduction of NiCo$_2$O$_x$/CeO$_2$ NR further substantiates the adsorption-electrocatalysis effect of NiCo$_2$O$_x$/CeO$_2$ NR. Moreover, the cell with NiCo$_2$O$_x$/CeO$_2$ NR showed reduced overpotential (η) of 0.18 V compared to the 0.20 V and 0.30 V of the cells with CeO$_2$ nanorods and bare CC respectively exhibiting accelerated redox reaction kinetics provided by the bimetallic NiCo$_2$O$_x$ electrocatalyst clustered on CeO$_2$ nanorods. The discharge curve of the cell can be divided into two sections called high plateau (Q$_H$) and low plateau (Q$_L$) corresponding to the higher order polysulfide (Li$_2$S$_x$: x > 4) dissolution and conversion of Li$_2$S$_4$ to Li$_2$S$_2$/Li$_2$S. The longer Q$_L$ of the cell with NiCo$_2$O$_x$/CeO$_2$ NR (Q$_L$ = 813 mAh g^{-1} for NiCoO$_x$/CeO$_2$, 645 mAh g^{-1} for CeO$_2$, 167 mAh g^{-1} for bare CC) and the high ratio Q$_L$/Q$_H$ for NiCo$_2$O$_x$/CeO$_2$ NR (1.92, which is 5.3 times higher than bare CC) manifest the effective redox conversion of polysulfides by providing electrocatalytic effect resulting in high sulfur utilization.

The cycle performances of NiCo$_2$O$_x$/CeO$_2$ NR and bare carbon cloth containing 1.33 mg cm^{-2} S loading at 0.2C were performed shown in Fig. 7c. The NiCo$_2$O$_x$/CeO$_2$ NR based cathode host can provide stable performance at 0.2C for 100 cycles and maintain a discharge capacity of 1120 mAh g^{-1}. On the contrary, the plain CC cathode host show unpromising capacity from 628 mAh g^{-1} to 674 mAh g^{-1} after 100 cycles. This verifies the efficacy of NiCo$_2$O$_x$/CeO$_2$ NR in catalytic redox kinetics and high-capacity retention of the battery. Furthermore, the average Coulombic efficiency was maintained over 99% confirming the mitigation of polysulfide shuttling effect and high sulfur utilization. The long-range cycle performance of NiCo$_2$O$_x$/CeO$_2$ NR was also investigated at high current

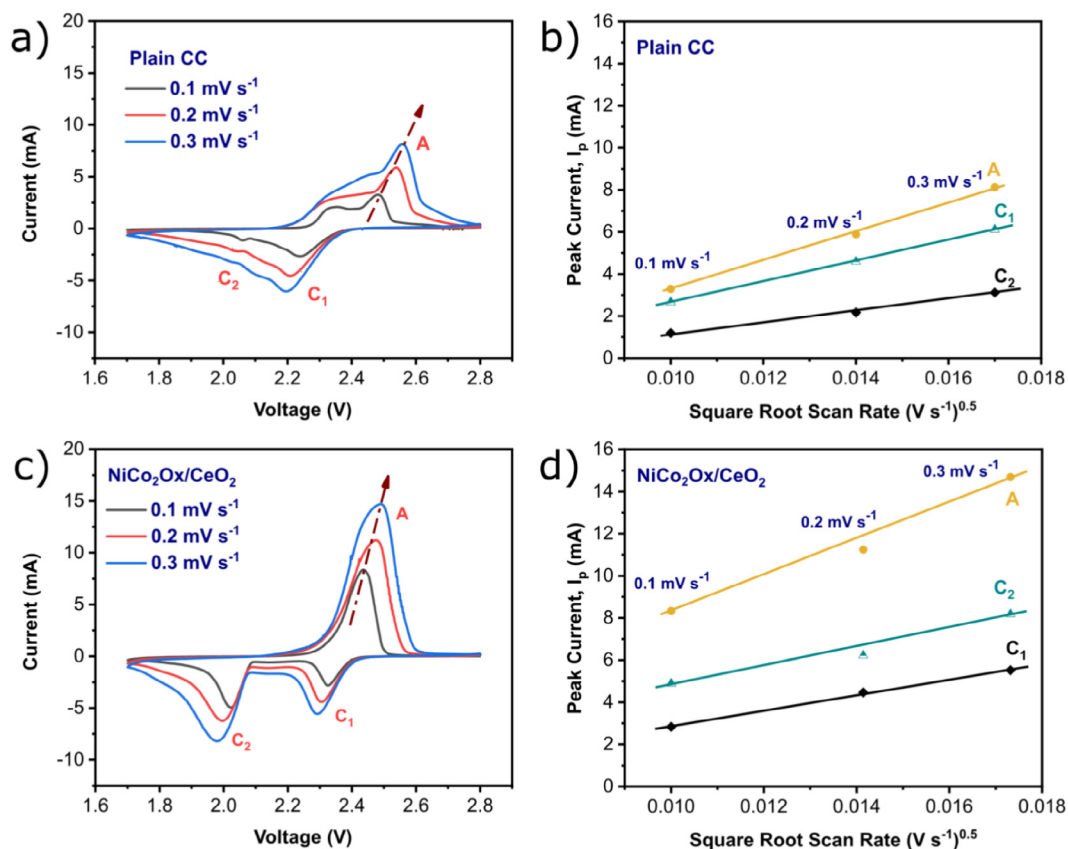**Fig. 6.** Asymmetric CV profiles at different scanning speeds for a) plain CC and c) $NiCo_2O_x/CeO_2$ NR and their corresponding linearly fitted curves of b) plain CC and d) $NiCo_2O_x/CeO_2$ NR respectively.

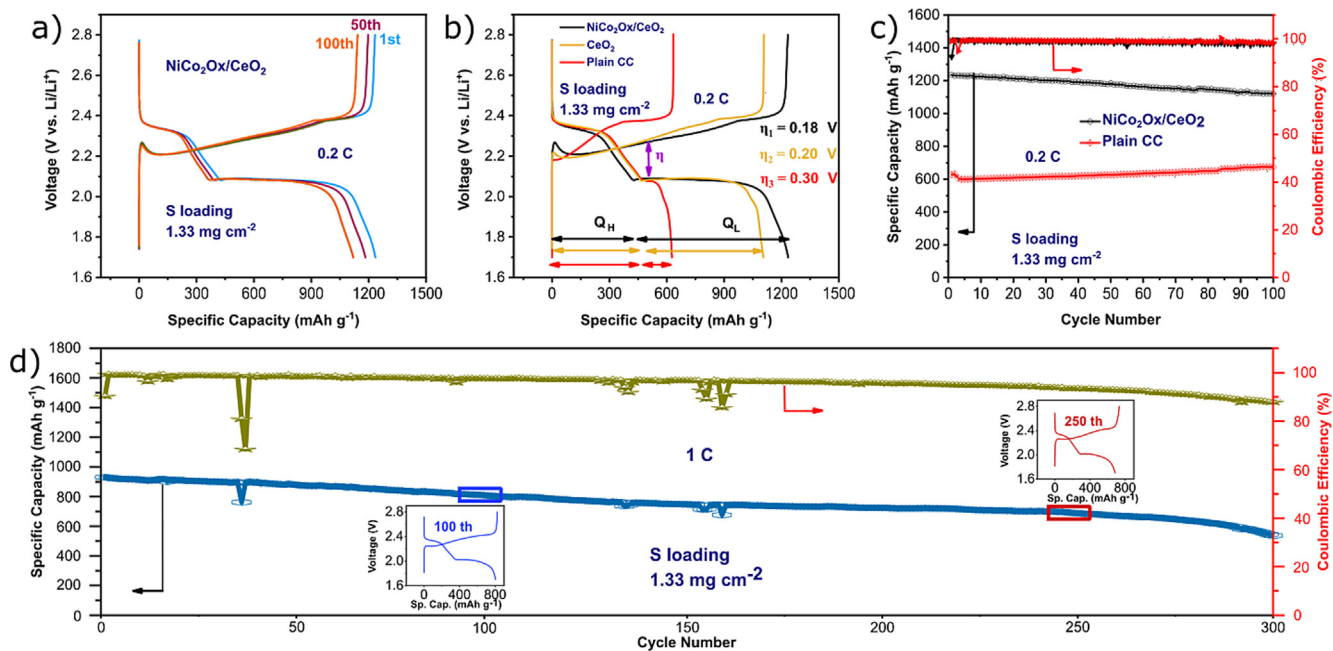**Fig. 7.** Electrochemical performance of batteries with $NiCo_2O_x/CeO_2$ NR and bare CC cathode host. a) Charge-discharge profile of LSB with $NiCo_2O_x/CeO_2$ NR at 0.2C between 1.7 and 2.8 V vs Li^+/Li. b) Performance comparison at 0.2C for LSB with $NiCo_2O_x/CeO_2$ NR, CeO_2 nanorods and plain CC. c) Cycle performance at 0.2C with and without $NiCo_2O_x/CeO_2$ NR cathode host. d) Long cycle performance at 1C with $NiCo_2O_x/CeO_2$ NR.

density of 1C as shown in Fig. 7d. The $NiCo_2O_x/CeO_2$ NR cathode host displays an initial discharge capacity of 931 mAh g^{-1} and reaches the capacity of 537 mAh g^{-1} after 300 cycles, with a capacity decay rate of only 0.14% per cycle. The inset figures in Fig. 7d

shows the charge discharge curve at 100th and 250th cycle, which maintains the long discharge plateau even after long cycling at high current density. The charge-discharge curves also remained stable with no apparent change in polarization, indicating homogenous distribution of Li_2S_2/Li_2S discharge products avoiding sulfur aggregation [70]. These capacity and cycle stability of the battery show significant improvement in LSB performance compared to CeO_2 host material as previously reported in several articles (Table 2).

Inspired by the excellent electrochemical performance of $NiCo_2O_x/CeO_2$ NR with 1.33 mg cm^{-2} sulfur loading, further galvanostatic charge discharge experiments were conducted with higher sulfur loading of 2.67 mg cm^{-2}. Fig. 8a gives the charge discharge curves for the cell with $NiCo_2O_x/CeO_2$ after different cycles at 0.2C. Even with higher sulfur loading, the two-plateau discharge behavior is obvious indicating restrained polysulfide shuttling effect. The smaller voltage polarization compared to the cell with bare CC still exists suggesting promotion of redox kinetics (Fig. 8b). This improved polarization contributes to higher energy efficiency which is crucial for designing industrial scale energy storage devices [100,101]. After cycling at current density of 0.2C with 2.67 mg cm^{-2} sulfur loading, the $NiCo_2O_x/CeO_2$ NR can achieve high initial capacity of 756 mAh g^{-1} with a reversible capacity of 657 mAh g^{-1} after 170 cycles with a capacity decay rate of only 0.08% per cycle (Fig. 8c). In comparison, the plain CC provides only 308 mAh g^{-1} due to the inefficient sulfur utilization. With a high current rate of 1C, as shown in Fig. 8d, the reversible discharge capacity of $NiCo_2O_x/CeO_2$ NR is 530 mAh g^{-1} and can be retained at about 501 mAh g^{-1} after 392 cycles, indicating negligible capacity decay of only 0.01% per cycle. In contrast, plain CC showed capacity of only 95 mAh g^{-1} after 392 cycles at 1C showing poor cycling performance at the sulfur loading of 2.67 mAhg^{-1}.

The adsorption-catalysis synergy towards catalytic redox polysulfide conversion enabled by $NiCo_2O_x/CeO_2$ is reflected in Fig. 9. The rate performances of $NiCo_2O_x/CeO_2$ NR and CeO_2 nanorods with 1.33 mg cm^{-2} sulfur loading were assessed with a current density range between 0.1C and 1C shown in Fig. 9a. $NiCo_2O_x/CeO_2$ NR could attain a high discharge capacity of 1434 mAh g^{-1} at 0.1C. When the current rate was modified to 0.2, 0.5 and 1C, the battery showed discharge capacities of 1307, 1185 and 1086 mAh g^{-1}, respectively. Following the current density inverted abruptly back to 0.5C and gradually to 0.1C, the specific capacity of $NiCo_2O_x/CeO_2$ NR battery maintained good reversibility indicating outstanding cycling stability of the battery. The cell with CeO_2 nanorods also showed excellent discharge capacities of 1218, 1050,

980 and 952 mAh g^{-1} at current densities of 0.1, 0.2, 0.5 and 1C, respectively. This data further provides insights on the influence of $NiCo_2O_x$ clustered onto the CeO_2 nanorods where $NiCo_2O_x$ provides the catalytic effect.

Before running the battery with $NiCo_2O_x/CeO_2$ NR at 1C as shown in Fig. 7d, the cell was run at different current rates to test the robustness of the battery. The charge-discharge profile for $NiCo_2O_x/CeO_2$ NR cathode host at different current rates are shown in Fig. 9b. For the current rate of 0.1, 0.2 and 0.5C, the charge-discharge curves almost overlap each other demonstrating negligible polarization and a good rate capability. All the charge-discharge curves demonstrated two distinct discharge plateaus and a wide charging curve matching the CV profiles. The decrease in capacity and the length of the discharge plateau with increasing current density could be ascribed by the kinetic overpotential at higher current densities. Even at high current density of 1C, the two-plateau discharge profile with a long second discharge plateau is visible. Moreover, these capacities at different current rates are almost 1.95–2.38 times higher compared to bare CC (Fig. 9c). The voltage difference between the cathode and anode peaks, i.e. polarization (η) of the battery with $NiCo_2O_x/CeO_2$ NR, is lower than the battery with bare CC for various current densities (Fig. 9d). This maintenance of lower voltage polarization with the increasing current rate indicates faster electrochemical redox kinetics.

To investigate the feasibility for practical application where high sulfur loading and low electrolyte to sulfur ratio is desired, the battery with $NiCo_2O_x/CeO_2$ NR was tested at different sulfur loading keeping the amount of $NiCo_2O_x/CeO_2$ NR constant (Fig. 9e). The calculated sulfur content and E/S ratio for different sulfur loading are given in **Table S2**. With the sulfur loading increased to 2.67, 4 and 5.33 mg cm^{-2}, the batteries showed areal discharge capacities of 2.01, 1.85, 2.46 mAh cm^{-2} (756, 463, 462 mAh g^{-1}) at 0.2C, respectively. After 100 cycles, the areal discharge capacities could be maintained at 1.70, 1.82 and 2.33 mAh cm^{-2} (638, 455, 437 mAh g^{-1}) for sulfur loading of 2.67, 4 and 5.33 mg cm^{-2} respectively signifying high sulfur utilization by $NiCo_2O_x/CeO_2$ NR. Furthermore, the charge-discharge profiles for $NiCo_2O_x/CeO_2$ NR battery still exhibit the conventional voltage plateaus even after 100 cycles (Fig. 9f) suggesting excellent cycling stability of the battery with $NiCo_2O_x/CeO_2$ NR under practical conditions. The electrolyte to sulfur ratio (E/S ratio) influences the electrochemical performance heavily, where for practical application, the goal is to keep E/S ratio under 5 μL mg^{-1}. Here, at high sulfur loading of 5.33 mg cm^{-2}, the E/S ratio is about 7.5 μL mg^{-1} which is considerably close to practical condition. So, the perfor-

Table 2
Electrochemical performances of $NiCo_2O_x/CeO_2$ NR cathode host compared with other CeO_2 based representative sulfur cathodes.

| Material	Sulfur loading mg/cm^2	Current rate (C)	Cycle Number	Initial capacity (mAhg^{-1})	Reversible capacity (mAhg^{-1})	Capacity decay rate (% per cycle)	Ref.
CeO_2@CNF	1–1.5	0.2 C	100	1444	740	0.48	[90]
S/Fe/CeO_2/CNT	1.1	0.2 C	100	1241	1003	0.19	[91]
CeO_2@G	1.20	0.2 Ag^{-1-}	50	1546	1001	0.71	[92]
CeO_2 webbed CNT	1.3–1.6	0.2 C	100	1033	723	0.235	[93]
PAN/CNF-CeO_2	1.2	0.2 C	200	1359	700	0.24	[94]
CeO_2/MMNC-S	1.4	0.2 C	200	1368	1066	0.11	[95]
NC@H-CeO_2	1.4	0.2 C	100	1336	1010	0.24	[51]
S@CeO_2/PG	–	0.2 C	–	1104	–	–	[96]
	1.05	1 C	500	710	348.6	0.068	
S/CeO_2/RGO	–	0.1 C	200	1054	792	0.12	[52]
CeO_2/RGO	2	0.1 C	100	1136	886	0.24	[97]
S/CS-CeO_2/PC	0.7–1	0.25	100	1242.6	663.3	0.466	[98]
			500		421	0.015	
CeO_2/GR-1.8	1	0.1 C	350	1488	789.4	0.13	[99]
CeO_2/CFP	1.33	0.2 C	300	1177	775	0.11	[55]
$NiCo_2O_x/CeO_2$ NR	1.33	0.2 C	100	1236	1120	0.09	This work
	2.67	0. 2C	170	756	657	0.08	
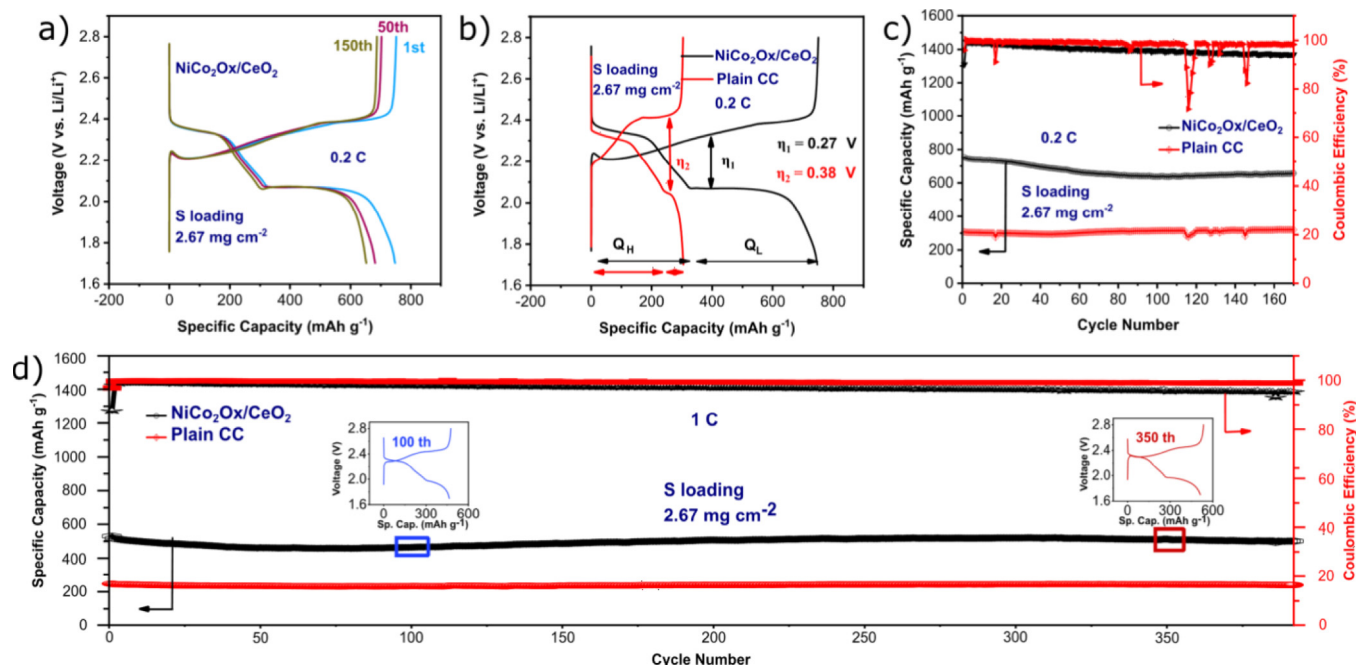
Fig. 8. Electrochemical performance of batteries with $NiCo_2O_x/CeO_2$ NR and bare CC cathode host with 2.67 mg cm^{-2} sulfur loading. a) The charge discharge profiles of $NiCo_2O_x/CeO_2$ at various cycles at 0.2C. b) Galvanostatic charge-discharge profile comparison of cells with $NiCo_2O_x/CeO_2$ NR and bare CC. c) Cycling performance of both batteries at 0.2C. d) Long term cycling performance of cells with and without $NiCo_2O_x/CeO_2$ NR at 1C.
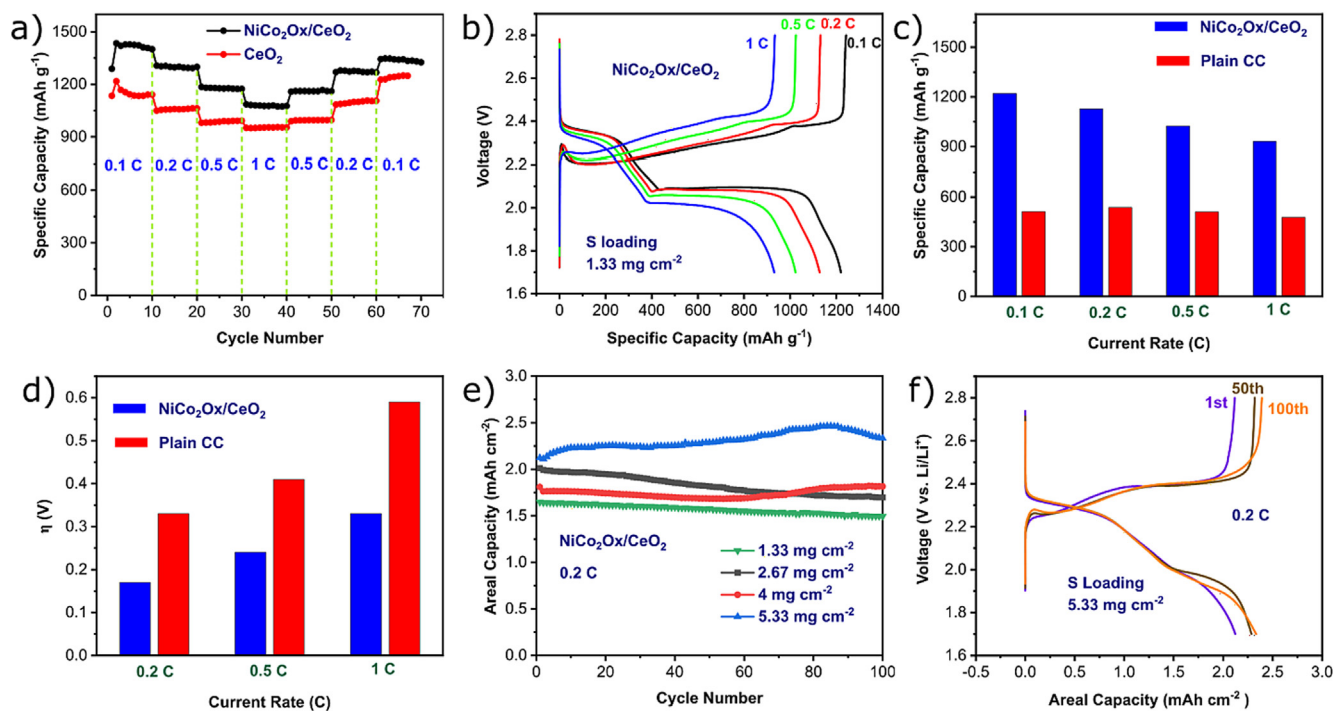

Fig. 9. a) Rate capability of LSB using $NiCo_2O_x/CeO_2$ NR and CeO_2 cathode host. b) Charge discharge curve at different current densities for LSB using $NiCo_2O_x/CeO_2$ NR. c) Capacity comparison between $NiCo_2O_x/CeO_2$ NR and bare CC at different current densities. d) Voltage polarization at different current rates. e) Cycle performance at different sulfur loadings at 0.2C. f) Galvanostatic charge-discharge curves with 5.33 mg cm^{-2} sulfur loading for various cycles.

mance needs improvement at lean electrolyte condition for $NiCo_2O_x/CeO_2$ NR for future research.

3.3. Microstructure analysis after cycling

The cells were disassembled inside an argon filled glovebox to conduct post cycling analysis. Fig. 10 **a-b** shows the morphological analysis of the Li foil for the batteries with bare CC and with $NiCo_2O_x/CeO_2$ NR respectively. It can be clearly seen that the Li anode

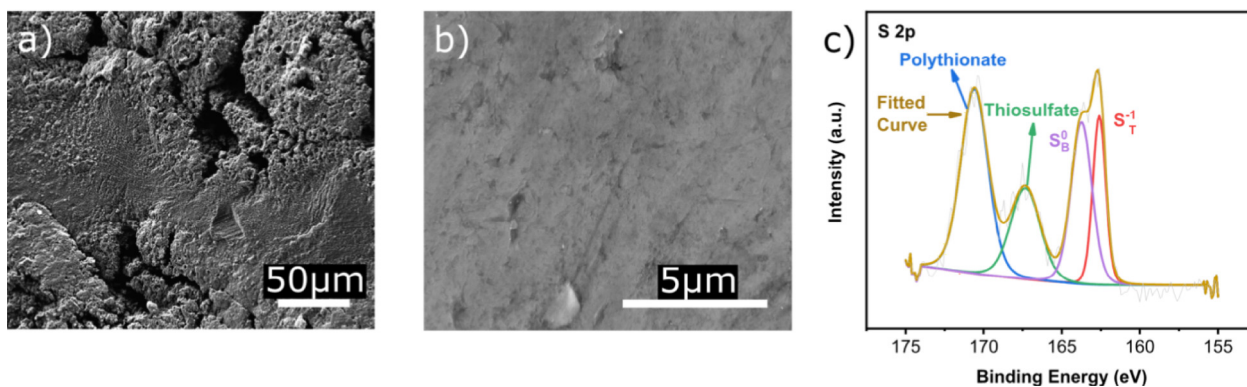**Fig. 10.** SEM images of cycled LSB anode for a) bare CC based cell and b) $NiCo_2O_x/CeO_2$ NR based cell. c) XPS S 2p spectrum for $NiCo_2O_x/CeO_2/CC$ cathode host after 100 galvanostatic charge-discharge cycles at 0.2C.

surface for the bare CC battery possesses rough surface with lots of pores and abundance of dead lithium. The rough surface could originate from the diffusion and deposition of soluble polysulfides on the Li anode. On the other hand, for the battery with $NiCo_2O_x/CeO_2$ NR the Li anode maintained surface smoothness without significant structural damage.

The XPS S 2p spectrum of the $NiCo_2O_x/CeO_2$ NR cathode host from the disassembled battery after galvanostatic charge-discharge for 100 cycles at 0.2C is shown in Fig. 10c. The XPS S 2p peak clearly shows the presence of polythionate complex ([SO_3-S_2SO_3]$^{2-}$) at the binding energy of 170.6 eV and the thiosulfate species ([S_2O_3]$^{2-}$) at 167.4 eV almost similar to the previously reported literatures [56,102,103]. Here, we assume that the $NiCo_2O_x/CeO_2$ NR oxidizes the long chain lithium polysulfides to produce thiosulfates, which further binds other emerging polysulfides and convert them into polythionates followed by reducing to insoluble Li_2S_2/Li_2S. This phenomenon accelerates the efficient conversion of lithium polysulfides resulting in high sulfur utilization [104]. Moreover, two S $2p_{3/2}$ contributions where the S_B^0 peak corresponding to the bridged S—S bond representing elemental sulfur at 163.8 eV and the S_T^{-1} corresponding to the terminal Li-S bond representing Li_2S_2/Li_2S at 162.6 eV are also visible [105]. The area under the curve for elemental sulfur (S_B^0) is about 1.55 times higher than the area under the curve for insoluble discharge product Li_2S (S_T^{-1}) which indicates efficient electrochemical conversion of lithium polysulfides.

Based on the above results and discussion, the mechanism of the synergistic effect for the high capacity of $NiCo_2O_x/CeO_2$ is as follows. The CeO_2 nanorods with abundant oxygen vacancy defect sites exposing (1 1 0)/(1 0 0) faces or defected (1 1 1) faces have reversible transition capability between Ce^{4+}/Ce^{3+} and can bind lithium polysulfides, whereas the highly conductive bimetallic $NiCo_2O_x$ exposes (3 1 1) plane to provide catalytic activity towards polysulfide conversion. From the post cycling XPS analysis of the $NiCo_2O_x/CeO_2$ NR cathode host, we methodically proved that the $NiCo_2O_x/CeO_2$ NR can strongly instigate the $S_2O_3^{2-}$ formation. These $S_2O_3^{2-}$ anchors with the S_x^{2-} (x = 4–8) of the higher order polysulfides and further serve as redox mediators by triggering the production of the intermediate form of polythionate complexes ([$SO_3S_2SO_3$]$^{2-}$). Then, it finally deconvolutes into S^{2-} as the final discharge product following the Wackenroder disproportionate reaction [106,107]. So, in sum, the $NiCo_2O_x/CeO_2$ NR helps the formation of $S_2O_3^{2-}$, thus initiating the Li_2S nucleation and catalytic conversion of polysulfides. The introduction of $NiCo_2O_x/CeO_2$ NR changes the regular discharge reaction of ($S_8 \rightarrow S_x^{2-} \rightarrow S^{2-}$) into ($S_8 \rightarrow S_x^{2-} + S_2O_3^{2-} \rightarrow [SO_3S_{x-2}SO_3]^{2-} \rightarrow S_xO_6^{2-} + S^{2-} \rightarrow S^{2-}$) accelerating the polysulfide transformation reaction [107]. Moreover, the

Li-ion transfers on the surface of $NiCo_2O_x/CeO_2$ NR due to low energy barrier to Li ion transfer.

4. Conclusion

In summary, we investigated the battery cell performance of CeO_2 nanorods supported bimetallic $NiCo_2O$ nanoparticles ($NiCo_2O_x/CeO_2$ NR) as efficient sulfur host for lithium sulfur battery to bind polysulfides and enhance the fast kinetic reaction in polysulfide conversion. The role of the CeO_2 nanorods here is to bind lithium polysulfides being a polar oxide host material, and the role of the bimetallic $NiCo_2O_x$ is to promote redox reaction kinetics by accelerating the polysulfide conversion, thus providing adsorption-catalysis dual synergy. The batteries with $NiCo_2O_x/CeO_2/CC$ cathode host exhibit an excellent specific capacity of 1236 mAh g^{-1} at 0.2C and maintains a specific capacity of 931 mAh g^{-1} at 1C. The capacity decay rate is only 0.09% per cycle at 0.2C after 100 cycles. Additionally, the battery can perform even in high sulfur loading of 5.33 mg cm^{-2} for practical application. Combining results from electrochemical characterization and post-mortem analysis, it can be concluded that the $NiCo_2O_x/CeO_2$ NR showed excellent performance and can be considered as a very promising candidate of cathode host material for lithium sulfur batteries.

Appendix A. Supplementary data

Supplementary data to this article can be found online at https://doi.org/10.1016/j.jcis.2022.12.130.

References

[1] M. Zhang, H. Du, Z. Wei, X. Zhang, R. Wang, Ultrafast Microwave Synthesis of Nickel-Cobalt Sulfide/Graphene Hybrid Electrodes for High-Performance Asymmetrical Supercapacitors, ACS Appl. Energy Mater. (2021).

[2] M. Zhang, H. Du, Z. Wei, X. Zhang, R. Wang, Facile Electrodeposition of Mn-CoP Nanosheets on Ni Foam as High-Rate and Ultrastable Electrodes for Supercapacitors, ACS Appl. Energy Mater. 5 (2021) 186–195.

[3] M. Zhang, A. Nautiyal, H. Du, Z. Wei, X. Zhang, R. Wang, Electropolymerization of polyaniline as high-performance binder free electrodes for flexible supercapacitor, Electrochim. Acta 376 (2021) 138037.

[4] P.G. Bruce, S.A. Freunberger, L.J. Hardwick, J.-M. Tarascon, Li–O2 and Li–S batteries with high energy storage, Nat. Mater. 11 (1) (2012) 19–29.

[5] X. Chen, T. Hou, K.A. Persson, Q. Zhang, Combining theory and experiment in lithium–sulfur batteries: current progress and future perspectives, Mater. Today 22 (2019) 142–158.

[6] Z. Li, H.B. Wu, X.W.D. Lou, Rational designs and engineering of hollow micro-/nanostructures as sulfur hosts for advanced lithium–sulfur batteries, Energ. Environ. Sci. 9 (10) (2016) 3061–3070.

[7] Y.V. Mikhaylik, J.R. Akridge, Polysulfide shuttle study in the Li/S battery system, J. Electrochem. Soc. 151 (11) (2004) A1969.

[8] J.-K. Sun, Q. Xu, Functional materials derived from open framework templates/precursors: synthesis and applications, Energ. Environ. Sci. 7 (7) (2014) 2071–2100.

[9] M. Zhang, W. Chen, L. Xue, Y. Jiao, T. Lei, J. Chu, J. Huang, C. Gong, C. Yan, Y. Yan, Y. Hu, X. Wang, J. Xiong, Adsorption-Catalysis Design in the Lithium-Sulfur Battery, Adv. Energy Mater. 10 (2) (2019).

[10] Y. Song, W. Cai, L. Kong, J. Cai, Q. Zhang, J. Sun, Rationalizing electrocatalysis of Li–S chemistry by mediator design: progress and prospects, Adv. Energy Mater. 10 (11) (2020) 1901075.

[11] X. Xu, S. Wang, H. Wang, B. Xu, C. Hu, Y. Jin, J. Liu, H. Yan, The suppression of lithium dendrite growth in lithium sulfur batteries: A review, J. Storage Mater. 13 (2017) 387–400.

[12] S.-H. Chung, A. Manthiram, Designing lithium-sulfur cells with practically necessary parameters, Joule 2 (4) (2018) 710–724.

[13] C. He, Y. Liang, W. Zhang, Design of Novel Transition-Metal-Doped C6N2 with High-Efficiency Polysulfide Anchoring and Catalytic Performances toward Application in Lithium-Sulfur Batteries, ACS Appl. Mater. Interfaces 14 (25) (2022) 29120–29130.

[14] T. Li, C. He, W. Zhang, Two-dimensional porous transition metal organic framework materials with strongly anchoring ability as lithium-sulfur cathode, Energy Storage Mater. 25 (2020) 866–875.

[15] T. Li, C. He, W. Zhang, Rational design of porous carbon allotropes as anchoring materials for lithium sulfur batteries, J. Energy Chem. 52 (2021) 121–129.

[16] X. Gao, Y. Huang, Z. Guang, X. Li, Constructing a multifunctional globular polypyrrole slurry cladding carbon aerogel/sulfur cathode for high-performance lithium–sulfur batteries, Energy Fuel 34 (3) (2020) 3931–3940.

[17] X. Gao, Y. Huang, Z. Zhang, S. Batool, X. Li, T. Li, Porous hollow carbon aerogel-assembled core@ polypyrrole nanoparticle shell as an efficient sulfur host through a tunable molecular self-assembly method for rechargeable lithium/sulfur batteries, ACS Sustain. Chem. Eng. 8 (42) (2020) 15822–15833.

[18] Y. Huang, X. Gao, X. Han, Z. Guang, X. Li, Controlled synthesis of three-dimensional porous carbon aerogel via catalysts: effects of morphologies toward the performance of lithium-sulfur batteries, Solid State Ion. 347 (2020) 115248.

[19] Z. Li, Y. Huang, L. Yuan, Z. Hao, Y. Huang, Status and prospects in sulfur–carbon composites as cathode materials for rechargeable lithium–sulfur batteries, Carbon 92 (2015) 41–63.

[20] Z.-L. Xu, J.-K. Kim, K. Kang, Carbon nanomaterials for advanced lithium sulfur batteries, Nano Today 19 (2018) 84–107.

[21] M. Zhu, S. Li, J. Liu, B. Li, Promoting polysulfide conversion by V2O3 hollow sphere for enhanced lithium-sulfur battery, Appl. Surf. Sci. 473 (2019) 1002–1008.

[22] G. Feng, X. Liu, Z. Wu, Y. Chen, Z. Yang, C. Wu, X. Guo, B. Zhong, W. Xiang, J. Li, Enhancing performance of Li–S batteries by coating separator with MnO @ yeast-derived carbon spheres, J. Alloy. Compd. 817 (2020) 152723.

[23] L. Fan, H. Wu, X. Wu, M. Wang, J. Cheng, N. Zhang, Y. Feng, K. Sun, Fe-MOF derived jujube pit like Fe3O4/C composite as sulfur host for lithium-sulfur battery, Electrochim. Acta 295 (2019) 444–451.

[24] J. Pu, Z. Shen, J. Zheng, W. Wu, C. Zhu, Q. Zhou, H. Zhang, F. Pan, Multifunctional Co 3 S 4 @sulfur nanotubes for enhanced lithium-sulfur battery performance, Nano Energy 37 (2017) 7–14.

[25] T. Chen, Z. Zhang, B. Cheng, R. Chen, Y. Hu, L. Ma, G. Zhu, J. Liu, Z. Jin, Self-Templated Formation of Interlaced Carbon Nanotubes Threaded Hollow Co3S4 Nanoboxes for High-Rate and Heat-Resistant Lithium-Sulfur Batteries, J. Am. Chem. Soc. 139 (36) (2017) 12710–12715.

[26] X. Li, Z. Pan, Z. Li, X. Wang, B. Saravanakumar, Y. Zhong, L. Xing, M. Xu, C. Guo, W. Li, Coral-like reduced graphene oxide/tungsten sulfide hybrid as a cathode host of high performance lithium-sulfur battery, J. Power Sources 420 (2019) 22–28.

[27] Q. Yuan, Y. Chen, A. Li, Y. Li, X. Chen, M. Jia, H. Song, Polysulfides anchoring and enhanced electrochemical kinetics of 3D flower-like FeS/carbon assembly materials for lithium-sulfur battery, Appl. Surf. Sci. 508 (2020).

[28] B. Moorthy, S. Kwon, J.H. Kim, P. Ragupathy, H.M. Lee, D.K. Kim, Tin sulfide modified separator as an efficient polysulfide trapper for stable cycling performance in Li-S batteries, Nanoscale Horiz 4 (1) (2019) 214–222.

[29] H. Shi, Z. Sun, W. Lv, S. Xiao, H. Yang, Y. Shi, K. Chen, S. Wang, B. Zhang, Q.-H. Yang, F. Li, Efficient polysulfide blocker from conductive niobium nitride@graphene for Li-S batteries, J. Energy Chem. 45 (2020) 135–141.

[30] J. He, A. Manthiram, Long-Life, High-Rate Lithium-Sulfur Cells with a Carbon-Free VN Host as an Efficient Polysulfide Adsorbent and Lithium Dendrite Inhibitor, Adv. Energy Mater. 10 (3) (2019).

[31] W. Xu, X. Pan, X. Meng, Z. Zhang, H. Peng, J. Liu, G. Li, A conductive sulfur-hosting material involving ultrafine vanadium nitride nanoparticles for high-performance lithium-sulfur battery, Electrochim. Acta 331 (2020).

[32] W. Zeng, M.M.C. Cheng, K.Y.S. Ng, Cathode Framework of Nanostructured Titanium Nitride/Graphene for Advanced Lithium-Sulfur Batteries, ChemElectroChem 6 (10) (2019) 2796–2804.

[33] H. Pan, K.S. Han, M.H. Engelhard, R. Cao, J. Chen, J.G. Zhang, K.T. Mueller, Y. Shao, J. Liu, Addressing passivation in lithium–sulfur battery under lean electrolyte condition, Adv. Funct. Mater. 28 (38) (2018) 1707234.

[34] X. Wu, N. Liu, M. Wang, Y. Qiu, B. Guan, D. Tian, Z. Guo, L. Fan, N. Zhang, A Class of Catalysts of BiOX (X = Cl, Br, I) for Anchoring Polysulfides and Accelerating Redox Reaction in Lithium Sulfur Batteries, ACS Nano 13 (11) (2019) 13109–13115.

[35] T. Lei, W. Chen, W. Lv, J. Huang, J. Zhu, J. Chu, C. Yan, C. Wu, Y. Yan, W. He, Inhibiting polysulfide shuttling with a graphene composite separator for highly robust lithium-sulfur batteries, Joule 2 (10) (2018) 2091–2104.

[36] Z. Du, X. Chen, W. Hu, C. Chuang, S. Xie, A. Hu, W. Yan, X. Kong, X. Wu, H. Ji, L.J. Wan, Cobalt in Nitrogen-Doped Graphene as Single-Atom Catalyst for High-Sulfur Content Lithium-Sulfur Batteries, J Am Chem Soc 141 (9) (2019) 3977–3985.

[37] R. Xu, J. Lu, K. Amine, Progress in mechanistic understanding and characterization techniques of Li-S batteries, Adv. Energy Mater. 5 (16) (2015) 1500408.

[38] Y. Feng, H. Liu, Q. Lu, Y. Liu, J. Li, X. He, X. Liu, D. Mikhailova, Designing hierarchical MnO/polypyrrole heterostructures to couple polysulfides adsorption and electrocatalysis in lithium-sulfur batteries, J. Power Sources 520 (2022) 230885.

[39] J. Liu, C. Lin, Q. Xie, D.-L. Peng, R.-J. Xie, Core–shell zeolite imidazole framework-derived ZnSe@ CoSe2/C heterostructure enabling robust polysulfide adsorption and rapid Li+ diffusion in high-rate and high-loading lithium–sulfur batteries, Chem. Eng. J. 430 (2022) 133099.

[40] J. Pu, W. Gong, Z. Shen, L. Wang, Y. Yao, G. Hong, CoNiO2/Co4N Heterostructure Nanowires Assisted Polysulfide Reaction Kinetics for Improved Lithium-Sulfur Batteries, Adv. Sci. 9 (4) (2022) 2104375.

[41] J. Pu, Z. Wang, P. Xue, K. Zhu, J. Li, Y. Yao, The effect of NiO-Ni3N interfaces in in-situ formed heterostructure ultrafine nanoparticles on enhanced polysulfide regulation in lithium-sulfur batteries, J. Energy Chem. 68 (2022) 762–770.

[42] C. Song, W. Zhang, Q. Jin, Y. Zhang, X. Wang, Z. Bakenov, In-situ constructed accordion-like Nb2C/Nb2O5 heterostructure as efficient catalyzer towards high-performance lithium-sulfur batteries, J. Power Sources 520 (2022) 230902.

[43] Z. Liu, J. Li, R. Wang, CeO2 nanorods supported M-Co bimetallic oxides (M=Fe, Ni, Cu) for catalytic CO and C3H8 oxidation, J Colloid Interface Sci 560 (2020) 91–102.

[44] Z. Liu, J. Li, M. Buettner, R.V. Ranganathan, M. Uddi, R. Wang, Metal-Support Interactions in CeO2- and SiO2-Supported Cobalt Catalysts: Effect of Support Morphology, Reducibility, and Interfacial Configuration, ACS Appl. Mater. Interfaces 11 (18) (2019) 17035–17049.

[45] C.T. Campbell, C.H. Peden, Oxygen vacancies and catalysis on ceria surfaces, Science 309 (5735) (2005) 713–714.

[46] H.-X. Mai, L.-D. Sun, Y.-W. Zhang, R. Si, W. Feng, H.-P. Zhang, H.-C. Liu, C.-H. Yan, Shape-selective synthesis and oxygen storage behavior of ceria nanopolyhedra, nanorods, and nanocubes, J. Phys. Chem. B 109 (51) (2005) 24380–24385.

[47] R. Wang, P.A. Crozier, R. Sharma, Structural transformation in ceria nanoparticles during redox processes, J. Phys. Chem. C 113 (14) (2009) 5700–5704.

[48] R. Wang, P.A. Crozier, R. Sharma, J.B. Adams, Measuring the redox activity of individual catalytic nanoparticles in cerium-based oxides, Nano Lett. 8 (3) (2008) 962–967.

[49] E. Mamontov, T. Egami, R. Brezny, M. Koranne, S. Tyagi, Lattice defects and oxygen storage capacity of nanocrystalline ceria and ceria-zirconia, J. Phys. Chem. B 104 (47) (2000) 11110–11116.

[50] A. Trovarelli, Catalytic properties of ceria and CeO2-containing materials, Catal. Rev. 38 (4) (1996) 439–520.

[51] W. Qi, W. Jiang, F. Xu, J. Jia, C. Yang, B. Cao, Improving confinement and redox kinetics of polysufides through hollow NC@CeO2 nanospheres for high-performance lithium-sulfur batteries, Chem. Eng. J. 382 (2020).

[52] Q. Hao, G. Cui, Y. Tian, T. Tan, Y. Zhang, Three-Dimensional S/CeO(2)/RGO Composites as Cathode Materials for Lithium(-)Sulfur Batteries, Materials (Basel) (2018) 11 (9).

[53] X. Qian, L. Jin, L. Zhu, S. Yao, D. Rao, X. Shen, X. Xi, K. Xiao, S. Qin, CeO2 nanodots decorated ketjen black for high performance lithium–sulfur batteries, RSC Adv. 6 (112) (2016) 111190–111196.

[54] Z. Wei, J. Li, Y. Wang, R. Wang, High-performance Li-S batteries enabled by polysulfide-infiltrated free-standing 3D carbon cloth with CeO2 nanorods decoration, Electrochim. Acta 388 (2021).

[55] S. Azam, Z. Wei, R. Wang, Cerium oxide nanorods anchored on carbon nanofibers derived from cellulose paper as effective interlayer for lithium sulfur battery, J. Colloid Interface Sci. 615 (2022) 417–431.

[56] Z. Wei, J. Li, R. Wang, Surface engineered polar CeO2-based cathode host materials for immobilizing lithium polysulfides in High-performance Li-S batteries, Appl. Surf. Sci. 580 (2022).

[57] Z. Wei, R. Wang, Chemically etched CeO2-x nanorods with abundant surface defects as effective cathode additive for trapping lithium polysulfides in Li-S batteries, J. Colloid Interface Sci. 615 (2022) 527–542.

[58] R. Wei, Y. Lu, Y. Xu, The role of oxygen vacancies in metal oxides for rechargeable ion batteries, Sci. China Chem. 64 (11) (2021) 1826–1853.

[59] Y. Li, P. Hasin, Y. Wu, NixCo3− xO4 nanowire arrays for electrocatalytic oxygen evolution, Adv. Mater. 22 (17) (2010) 1926–1929.

[60] Y. Chen, Q. Zhang, Z. Zhang, X. Zhou, Y. Zhong, M. Yang, Z. Xie, J. Wei, Z. Zhou, Two better than one: cobalt–copper bimetallic yolk–shell nanoparticles supported on graphene as excellent cathode catalysts for Li–O 2 batteries, J. Mater. Chem. A 3 (34) (2015) 17874–17879.

[61] A. Pendashteh, M.S. Rahmanifar, R.B. Kaner, M.F. Mousavi, Facile synthesis of nanostructured CuCo 2 O 4 as a novel electrode material for high-rate supercapacitors, Chem. Commun. 50 (16) (2014) 1972–1975.

[62] B. Liu, B. Liu, Q. Wang, X. Wang, Q. Xiang, D. Chen, G. Shen, New energy storage option: toward ZnCo2O4 nanorods/nickel foam architectures for high-performance supercapacitors, ACS Appl. Mater. Interfaces 5 (20) (2013) 10011–10017.

[63] B. Zhu, S. Tang, S. Vongehr, H. Xie, J. Zhu, X. Meng, FeCo 2 O 4 submicron-tube arrays grown on Ni foam as high rate-capability and cycling-stability electrodes allowing superior energy and power densities with symmetric supercapacitors, Chem. Commun. 52 (12) (2016) 2624–2627.

[64] X. He, R. Li, J. Liu, Q. Liu, D. Song, J. Wang, Hierarchical FeCo2O4@ NiCo layered double hydroxide core/shell nanowires for high performance flexible all-solid-state asymmetric supercapacitors, Chem. Eng. J. 334 (2018) 1573–1583.

[65] Q. Zhou, J. Xing, Y. Gao, X. Lv, Y. He, Z. Guo, Y. Li, Ordered assembly of NiCo2O4 multiple hierarchical structures for high-performance pseudocapacitors, ACS Appl. Mater. Interfaces 6 (14) (2014) 11394–11402.

[66] X. Hou, X. Wang, B. Liu, Q. Wang, T. Luo, D. Chen, G. Shen, Hierarchical MnCo 2 O 4 nanosheet arrays/carbon cloths as integrated anodes for lithium-ion batteries with improved performance, Nanoscale 6 (15) (2014) 8858–8864.

[67] G. Li, L. Xu, Y. Zhai, Y. Hou, Fabrication of hierarchical porous MnCo 2 O 4 and CoMn 2 O 4 microspheres composed of polyhedral nanoparticles as promising anodes for long-life LIBs, J. Mater. Chem. A 3 (27) (2015) 14298–14306.

[68] M. Li, W. Feng, W. Su, C. Song, L. Cheng, MOF-derived hollow cage Ni–Co mixed oxide/CNTs nanocomposites with enhanced electrochemical performance for lithium–sulfur batteries, Ionics 25 (9) (2019) 4037–4045.

[69] Y.T. Liu, D.D. Han, L. Wang, G.R. Li, S. Liu, X.P. Gao, NiCo2O4 nanofibers as carbon-free sulfur immobilizer to fabricate sulfur-based composite with high volumetric capacity for lithium–sulfur battery, Adv. Energy Mater. 9 (11) (2019) 1803477.

[70] J. Pu, W. Gong, Z. Shen, L. Wang, Y. Yao, G. Hong, CoNiO2 /Co4 N Heterostructure Nanowires Assisted Polysulfide Reaction Kinetics for Improved Lithium-Sulfur Batteries, Adv. Sci. (Weinh) 9 (4) (2022) e2104375.

[71] H. Zhang, G. Liu, L. Shi, J. Ye, Adv. Energy Mater. 8 (2018) 1701343; c) A. Wang, J. Li, T. Zhang. Nat. Rev. Chem. 2 (2018) 65-81.

[72] Y.C. Jiang, H.M.U. Arshad, H.J. Li, S. Liu, G.R. Li, X.P. Gao, Crystalline Multi-Metallic Compounds as Host Materials in Cathode for Lithium-Sulfur Batteries, Small 17 (22) (2021) e2005332.

[73] X. Lv, T. Lei, B. Wang, W. Chen, Y. Jiao, Y. Hu, Y. Yan, J. Huang, J. Chu, C. Yan, C. Wu, J. Wang, X. Niu, J. Xiong, An Efficient Separator with Low Li-Ion Diffusion Energy Barrier Resolving Feeble Conductivity for Practical Lithium-Sulfur Batteries, Adv. Energy Mater. 9 (40) (2019).

[74] X. Zhang, Y. Fan, M.A. Khan, H. Zhao, D. Ye, J. Wang, B. Yue, J. Fang, J. Xu, L. Zhang, J. Zhang, Co−Ni Binary-Metal Oxide Coated with Porous Carbon Derived from Metal-Organic Framework as Host of Nano-Sulfur for Lithium-Sulfur Batteries, Batteries & Supercaps 3 (1) (2019) 108−116.

[75] Y.T. Liu, D.D. Han, L. Wang, G.R. Li, S. Liu, X.P. Gao, NiCo 2 O 4 Nanofibers as Carbon-Free Sulfur Immobilizer to Fabricate Sulfur-Based Composite with High Volumetric Capacity for Lithium-Sulfur Battery, Adv. Energy Mater. 9 (11) (2019).

[76] A. Iqbal, Z.A. Ghazi, A.M. Khattak, A. Ahmad, Efficient sulfur host based on NiCo2O4 hollow microtubes for advanced Li-S batteries, J. Solid State Chem. 256 (2017) 189–195.

[77] R. Wang, R. Dangerfield, Seed-mediated synthesis of shape-controlled CeO 2 nanocrystals, RSC Adv. 4 (7) (2014) 3615–3620.

[78] S.T. Hossain, E. Azeeva, K. Zhang, E.T. Zell, D.T. Bernard, S. Balaz, R. Wang, A comparative study of CO oxidation over Cu-O-Ce solid solutions and CuO/CeO2 nanorods catalysts, Appl. Surf. Sci. 455 (2018) 132–143.

[79] B. Choudhury, P. Chetri, A. Choudhury, Oxygen defects and formation of Ce 3+ affecting the photocatalytic performance of CeO 2 nanoparticles, RSC Adv. 4 (9) (2014) 4663–4671.

[80] C. Schilling, A. Hofmann, C. Hess, M.V. Ganduglia-Pirovano, Raman spectra of polycrystalline CeO2: a density functional theory study, J. Phys. Chem. C 121 (38) (2017) 20834–20849.

[81] Y. Peng, C. Wang, J. Li, Structure–activity relationship of VOx/CeO2 nanorod for NO removal with ammonia, Appl. Catal. B 144 (2014) 538–546.

[82] W. Qi, W. Jiang, F. Xu, J. Jia, C. Yang, B. Cao, Improving confinement and redox kinetics of polysufides through hollow NC@ CeO2 nanospheres for high-performance lithium-sulfur batteries, Chem. Eng. J. 382 (2020) 122852.

[83] W. Zou, C. Ge, M. Lu, S. Wu, Y. Wang, J. Sun, Y. Pu, C. Tang, F. Gao, L. Dong, Engineering the NiO/CeO 2 interface to enhance the catalytic performance for CO oxidation, RSC Adv. 5 (119) (2015) 98335–98343.

[84] X. Dai, K. Zou, W. Jing, P. Xu, J. Sun, S. Guo, Q. Tan, Y. Liu, T. Zhou, Y. Chen, A dual-functional interlayer for Li–S batteries using carbon fiber film cladded electron-deficient Li2B4O7, J. Mater. Chem. A 10 (30) (2022) 16152–16162.

[85] Z. Liu, Y. Lu, M.P. Confer, H. Cui, J. Li, Y. Li, Y. Wang, S.C. Street, E.K. Wujcik, R. Wang, Thermally Stable RuOx–CeO2 Nanofiber Catalysts for Low-Temperature CO Oxidation, ACS Appl. Nano Mater. 3 (8) (2020) 8403–8413.

[86] Z. Wei, R. Wang, Chemically etched CeO(2−x) nanorods with abundant surface defects as effective cathode additive for trapping lithium polysulfides in Li-S batteries, J. Colloid Interface Sci. 615 (2022) 527–542.

[87] K. Zou, T. Zhou, Y. Chen, X. Xiong, W. Jing, X. Dai, M. Shi, N. Li, J. Sun, S. Zhang, C. Zhang, Y. Liu, Z. Guo, Defect Engineering in a Multiple Confined Geometry for Robust Lithium-Sulfur Batteries, Adv. Energy Mater. 12 (18) (2022).

[88] X. Wu, X. Liu, S. Yao, S. Li, S. Pang, X. Shen, T. Li, S. Qin, Boosting the electrochemical performance of lithium-sulfur batteries by using a carbon black/LiMn2O4-modified separator, J. Alloy. Compd. 835 (2020) 155251.

[89] X. Zhang, L. Zhu, Z. Gao, L. Zhang, Z. Zhang, L. Zhang, Y. Wang, Decoration of carbon nanofibers with bimetal sulfides as interlayer for high performance lithium-sulfur battery, Mater. Today Commun. 28 (2021).

[90] H. Wang, B. Zhang, X. Zeng, L. Yan, J. Zheng, M. Ling, Y. Hou, Y. Lu, C. Liang, 3D porous carbon nanofibers with CeO2-decorated as cathode matrix for high performance lithium-sulfur batteries, J. Power Sources 473 (2020).

[91] T. Wang, D. Su, Y. Chen, K. Yan, L. Yu, L. Liu, Y. Zhong, P.H.L. Notten, C. Wang, G. Wang, Biomimetic 3D Fe/CeO2 decorated N-doped carbon nanotubes architectures for high-performance lithium-sulfur batteries, Chem. Eng. J. 401 (2020).

[92] P. Cheng, P. Guo, K. Sun, Y. Zhao, D. Liu, D. He, CeO2 decorated graphene as separator modification material for capture and boost conversion of polysulfide in lithium-sulfur batteries, J. Membr. Sci. 619 (2021).

[93] D. Xiao, C. Lu, C. Chen, S. Yuan, CeO2-webbed carbon nanotubes as a highly efficient sulfur host for lithium-sulfur batteries, Energy Storage Mater. 10 (2018) 216–222.

[94] J. Zhang, Q. Rao, B. Jin, J. Lu, Q.-G. He, Y. Hou, Z. Li, X. Zhan, F. Chen, Q. Zhang, Cerium oxide embedded bilayer separator enabling fast polysulfide conversion for high-performance lithium-sulfur batteries, Chem. Eng. J. 388 (2020).

[95] L. Ma, R. Chen, G. Zhu, Y. Hu, Y. Wang, T. Chen, J. Liu, Z. Jin, Cerium Oxide Nanocrystal Embedded Bimodal Micromesoporous Nitrogen-Rich Carbon Nanospheres as Effective Sulfur Host for Lithium-Sulfur Batteries, ACS Nano 11 (7) (2017) 7274–7283.

[96] M. Kim, J. Lee, Y. Jeon, Y. Piao, Phosphorus-doped graphene nanosheets anchored with cerium oxide nanocrystals as effective sulfur hosts for high performance lithium-sulfur batteries, Nanoscale 11 (29) (2019) 13758–13766.

[97] S. Wang, F. Gao, Y. Zhao, N. Liu, T. Tan, X. Wang, Two-Dimensional CeO2/RGO Composite-Modified Separator for Lithium/Sulfur Batteries, Nanoscale Res Lett 13 (1) (2018) 377.

[98] X. Chen, L. Li, Y. Shan, D. Zhou, W. Cui, Y. Zhao, Synergistic effect of cerium oxide with core-shell structure embedded in porous carbon for high-performance lithium-sulfur batteries, Mater. Today Commun. (2021) 27.

[99] F. Zhu, M. Zhang, X. Cao, CeO2/GR interlayer prepared to reinforce the cathode and promote the electrochemical performance of lithium-sulfur batteries, Synth. Met. 282 (2021).

[100] Z. Yuan, H.-J. Peng, T.-Z. Hou, J.-Q. Huang, C.-M. Chen, D.-W. Wang, X.-B. Cheng, F. Wei, Q. Zhang, Powering lithium–sulfur battery performance by propelling polysulfide redox at sulfiphilic hosts, Nano Lett. 16 (1) (2016) 519–527.

[101] M.-E. Zhong, J. Guan, Q. Feng, X. Wu, Z. Xiao, W. Zhang, S. Tong, N. Zhou, D. Gong, Accelerated polysulfide redox kinetics revealed by ternary sandwich-type S@Co/N-doped carbon nanosheet for high-performance lithium-sulfur batteries, Carbon 128 (2018) 86–96.

[102] D.K. Lee, Y. Chae, H. Yun, C.W. Ahn, J.W. Lee, CO2-Oxidized Ti3C2T x–MXenes Components for Lithium-Sulfur Batteries: Suppressing the Shuttle Phenomenon through Physical and Chemical Adsorption, ACS Nano 14 (8) (2020) 9744–9754.

[103] W. Yao, W. Zheng, J. Xu, C. Tian, K. Han, W. Sun, S. Xiao, ZnS-SnS@ NC Heterostructure as robust lithiophilicity and sulfiphilicity mediator toward high-rate and long-life lithium–sulfur batteries, ACS Nano 15 (4) (2021) 7114–7130.

[104] X. Liang, C. Hart, Q. Pang, A. Garsuch, T. Weiss, L.F. Nazar, A highly efficient polysulfide mediator for lithium-sulfur batteries, Nat. Commun. 6 (2015) 5682.

[105] B. Li, Q. Su, L. Yu, J. Zhang, G. Du, D. Wang, D. Han, M. Zhang, S. Ding, B. Xu, Tuning the band structure of MoS2 via Co9S8@ MoS2 core–shell structure to boost catalytic activity for lithium–sulfur batteries, ACS Nano 14 (12) (2020) 17285–17294.

[106] X. Liang, C.Y. Kwok, F. Lodi-Marzano, Q. Pang, M. Cuisinier, H. Huang, C.J. Hart, D. Houtarde, K. Kaup, H. Sommer, T. Brezesinski, J. Janek, L.F. Nazar, Tuning Transition Metal Oxide-Sulfur Interactions for Long Life Lithium Sulfur Batteries: The "Goldilocks" Principle, Adv. Energy Mater. 6 (6) (2016).

[107] J. Xia, R. Gao, Y. Yang, Z. Tao, Z. Han, S. Zhang, Y. Xing, P. Yang, X. Lu, G. Zhou, TinO2n-1/MXene Hierarchical Bifunctional Catalyst Anchored on Graphene Aerogel toward Flexible and High-Energy Li-S Batteries, ACS Nano (2022).